AGU100 ADVANCING EARTH AND SPACE SCIENCE

JGR

Journal of Geophysical Research: Atmospheres

RESEARCH ARTICLE

10.1029/2018JD028271

Special Section:
Deep Convective Clouds and Chemistry 2012 Studies (DC3)

Key Points:
- Methyl hydroperoxide mixing ratios are decreased mainly by entrainment and liquid phase and mixed-phase scavenging
- Hydrogen peroxide and formaldehyde mixing ratios affected more by liquid phase scavenging than by entrainment or aqueous chemistry
- Overestimated rain/hail production in WRF-Chem reduces confidence in ice retention fraction values determined for peroxides and formaldehyde

Supporting Information:
- Supporting Information S1

Correspondence to:
M. M. Bela,
megan.bela@noaa.gov

Citation:
Bela, M. M., Barth, M. C., Toon, O. B., Fried, A., Ziegler, C., Cummings, K. A., et al. (2018). Effects of scavenging, entrainment, and aqueous chemistry on peroxides and formaldehyde in deep convective outflow over the central and Southeast United States. *Journal of Geophysical Research: Atmospheres*, *123*, 7594–7614. https://doi.org/10.1029/2018JD028271

Received 2 JAN 2018
Accepted 2 JUN 2018
Accepted article online 9 JUN 2018
Published online 19 JUL 2018

Effects of Scavenging, Entrainment, and Aqueous Chemistry on Peroxides and Formaldehyde in Deep Convective Outflow Over the Central and Southeast United States

Megan M. Bela[1,2,3,4], Mary C. Barth[5], Owen Brian Toon[1,2], Alan Fried[6], Conrad Ziegler[7], Kristin A. Cummings[8,9], Yunyao Li[8], Kenneth E. Pickering[8,10], Cameron R. Homeyer[11], Hugh Morrison[5], Qing Yang[12], Retha M. Mecikalski[13], Larry Carey[13], Michael I. Biggerstaff[11], Daniel P. Betten[11], and A. Addison Alford[11]

[1]Department of Atmospheric and Oceanic Sciences, University of Colorado Boulder, Boulder, CO, USA, [2]Laboratory for Atmospheric and Space Physics, University of Colorado Boulder, Boulder, CO, USA, [3]Cooperative Institute for Research in the Environmental Sciences, University of Colorado Boulder, Boulder, CO, USA, [4]Chemical Sciences Division, Earth System Research Laboratory, National Oceanic and Atmospheric Administration, Boulder, CO, USA, [5]National Center for Atmospheric Research, Boulder, CO, USA, [6]Institute of Arctic and Alpine Research, University of Colorado Boulder, Boulder, CO, USA, [7]National Severe Storms Laboratory, National Oceanic and Atmospheric Administration, Norman, OK, USA, [8]Department of Atmospheric and Oceanic Science, University of Maryland, College Park, MD, USA, [9]Kennedy Space Center, National Aeronautics and Space Administration, Merritt Island, FL, USA, [10]Goddard Space Flight Center, National Aeronautics and Space Administration, Greenbelt, MD, USA, [11]School of Meteorology, University of Oklahoma, Norman, OK, USA, [12]Pacific Northwest National Laboratory, Richland, WA, USA, [13]Department of Atmospheric Science, University of Alabama, Huntsville, AL, USA

Abstract Deep convective transport of gaseous precursors to ozone (O_3) and aerosols to the upper troposphere is affected by liquid phase and mixed-phase scavenging, entrainment of free tropospheric air and aqueous chemistry. The contributions of these processes are examined using aircraft measurements obtained in storm inflow and outflow during the 2012 Deep Convective Clouds and Chemistry (DC3) experiment combined with high-resolution ($dx \leq 3$ km) WRF-Chem simulations of a severe storm, an air mass storm, and a mesoscale convective system (MCS). The simulation results for the MCS suggest that formaldehyde (CH_2O) is not retained in ice when cloud water freezes, in agreement with previous studies of the severe storm. By analyzing WRF-Chem trajectories, the effects of scavenging, entrainment, and aqueous chemistry on outflow mixing ratios of CH_2O, methyl hydroperoxide (CH_3OOH), and hydrogen peroxide (H_2O_2) are quantified. Liquid phase microphysical scavenging was the dominant process reducing CH_2O and H_2O_2 outflow mixing ratios in all three storms. Aqueous chemistry did not significantly affect outflow mixing ratios of all three species. In the severe storm and MCS, the higher than expected reductions in CH_3OOH mixing ratios in the storm cores were primarily due to entrainment of low-background CH_3OOH. In the air mass storm, lower CH_3OOH and H_2O_2 scavenging efficiencies (SEs) than in the MCS were partly due to entrainment of higher background CH_3OOH and H_2O_2. Overestimated rain and hail production in WRF-Chem reduces the confidence in ice retention fraction values determined for the peroxides and CH_2O.

1. Introduction

Deep convective transport of gaseous precursors to ozone (O_3) and aerosols is an important source of O_3 and aerosol production in the upper troposphere (UT), where O_3 and aerosols affect the radiative forcing (Martini et al., 2011) and downwind air quality (Betts et al., 2002; Gerken et al., 2016). O_3 is produced in the upper troposphere from a suite of photochemical reactions involving hydrogen oxides (HO_x), nitrogen oxides (NO_x), and their precursors (primarily volatile organic compounds, VOCs). Due to the short lifetime of HO_x in the UT, the UT abundance of HO_x is controlled by the convective transport of HO_x precursors. HO_x precursors such as CH_2O, CH_3OOH, and H_2O_2 partition into cloud water and chemically transform, resulting in a fraction of these trace gases being removed by precipitation.

Aircraft observations in thunderstorm inflow and outflow regions during the 2012 Deep Convective Clouds and Chemistry (DC3) campaign enable the examination of convective transport in storms that formed in different dynamic and chemical environments. Fried et al. (2016) calculated CH_2O SEs ranging from 41% to 58% for DC3 storms. Barth et al. (2016) determined SEs varying from 79% to 97% for H_2O_2 and from 12% to 84% for CH_3OOH, in contrast to the expected CH_3OOH SEs of less than 10% based on aircraft measurements from previous field campaigns (e.g., Snow et al., 2007) and the low solubility of CH_3OOH. CH_3OOH SEs were lower for storms with more entrainment, and Barth et al. (2016) hypothesized that CH_3OOH was being replenished by entrainment of CH_3OOH from the free troposphere. In addition, cloud-resolving simulations of a severe storm from DC3 showed that ice retention (the process by which soluble species are retained in ice when cloud drops freeze) may also play a significant role in the removal of CH_3OOH (ice retention fraction, $r_f > 0.5$, determined by conducting multiple simulations with different r_f values and identifying the simulation for which SEs agreed with those calculated from observations), but not of CH_2O and H_2O_2 ($r_f < 0.25$) (Barth et al., 2016; Bela et al., 2016; Fried et al., 2016). However, Bela et al. (2016) hypothesized that the ice retention assumptions could have been compensating for the lack of aqueous chemistry in the model. For example, if gas phase mixing ratios of CH_2O decreased due to aqueous oxidation of CH_2O by the hydroxyl radical (OH) to produce formic acid (HCOOH), the r_f value used in the simulation could be artificially decreased to remove less CH_2O during cloud drop freezing and produce the correct net CH_2O transport. In a comparison of seven cloud chemistry box models, CH_2O and CH_3OOH mixing ratios were substantially lower and H_2O_2 mixing ratios were significantly higher in cloudy than clear air (Barth et al., 2003). Therefore, in the present study we investigate in greater detail ice retention for CH_2O, H_2O_2, and CH_3OOH and analyze in addition to the severe storm two other types of convection observed during DC3.

Theoretical studies have linked ice retention fractions to species solubility and details of the freezing process. Retention fractions for hydrometeor surfaces with temperatures above freezing (wet growth riming) are likely lower (e.g., $r_f(\mathrm{i} \rightarrow \mathrm{l}) < 0.2$, where $r_f(\mathrm{i} \rightarrow \mathrm{l})$ refers to the fraction remaining in the ice core to that in the liquid (Michael & Stuart, 2009)) than for below freezing hydrometeor surfaces (dry growth riming) because in wet growth riming, species are preferentially expelled from the frozen portion of the hydrometeor interior into the quasi-liquid surface layer. Dry growth riming ice retention fractions have been measured in laboratory and field experiments (e.g., $r_f = 0.05–1.0$ for H_2O_2, Jost et al., 2017; Iribarne & Pyshnov, 1990; Snider et al., 1992; Snider & Huang, 1998; Voisin et al., 2000; von Blohn et al., 2011, 2013). Ice retention of species that dissociate or react in cloud water can be affected by the reaction kinetics. For example, Jost et al. (2017) determined an average r_f value (the ratio of the concentration in the rime ice versus the liquid phase concentration in the supercooled cloud droplets prior to riming) of 0.97 for CH_2O, which they attribute to the diol ($CH_2(OH)_2$) formed by aqueous CH_2O not being able to dehydrate before the drop freezes. In the WRF-Chem simulations in this study, diol formation is included in the effective Henry's law coefficient for CH_2O because of the rapid formation of the diol.

Model simulations combined with aircraft measurements can be utilized to determine r_f values that result in simulated gas mixing ratios in convective outflow consistent with observations. While the laboratory studies can report r_f for single processes (e.g., dry-growth riming, Jost et al., 2017), the combined model simulations and aircraft measurements approach encompasses several processes that occur within the storm, including scavenging, entrainment, and chemistry. Thus, differences between the theoretical and laboratory studies with the field observations may be reconciled based on multiple processes affecting the trace gases. For example, using a one-dimensional plume model of tropical deep convection, Mari et al. (2000) showed that H_2O_2 was enhanced in convective outflow while HNO_3 was depleted, because H_2O_2 was not retained in ice during riming. Salzmann et al. (2007) found that for a highly soluble tracer the sensitivity of the deep convective tracer transport to the retention coefficient depends strongly on the initial profile and that tracers with a source in the free troposphere might be more sensitive to the retention coefficient. Furthermore, UT mixing ratios of highly retained trace gases with sources in the middle and upper troposphere were also sensitive to retention. Sensitivity simulations by Barth et al. (2007) with a 3-D thunderstorm model showed that when species are completely degassed, they are transported to the UT, while those retained in frozen hydrometeors are removed from the UT by snow and hail.

In this paper, we use aircraft and radar observations from DC3 combined with high-resolution Weather Research and Forecasting model with Chemistry (WRF-Chem, Grell et al., 2005; Fast et al., 2006) simulations to gain more insight into how ice retention interacts with other microphysical, dynamical, and chemical processes affecting reductions in mixing ratios of CH_3OOH, CH_2O, and H_2O_2. We focus our analysis on storms

in Oklahoma and Alabama and a mesoscale convective system (MCS) over Arkansas/Missouri/Illinois/Mississippi because these storms have been successfully simulated with WRF-Chem (Bela et al., 2016; Li et al., 2017; Phoenix et al., 2017; Yang et al., 2015); because the three storms differ greatly in updraft velocities, storm intensity, storm size, and other factors; and because we can build upon findings from semiidealized modeling studies (e.g., Barth et al., 2007; Mari et al., 2000; Salzmann et al., 2007) and DC3 (Barth et al., 2016; Bela et al., 2016; Fried et al., 2016).

SEs derived from observations use trace gas mixing ratios in storm inflow and outflow regions plus the entrainment rate. In the WRF-Chem simulations, the amount of scavenging depends on the production rate of rain, snow, and graupel from cloud water and ice (rainprod) minus evaporation (evapprod) ($\text{precip}_{\text{new}}$, cm^3 $H_2O\text{cm}^{-3}$ air) at each model level (z) during a time step (Δt, s):

$$\text{precip}_{\text{new}}(z) = (\text{rainprod}(z) - \text{evapprod}(z))\Delta t \tag{1}$$

In addition, the amount of WRF-Chem scavenging depends on the r_f value, the effective Henry's law solubility constant (H_{eff}, $\text{mol} \cdot \text{L}^{-1} \cdot \text{atm}^{-1}$), the gas phase mixing ratio (A_g, ppbv), and $\text{precip}_{\text{new}}$:

$$\text{SE} \propto \sum_{z=z_{\text{CB}}}^{z_{-15^\circ C}} r_f H_{\text{eff}}(z) A_g(z) \text{precip}_{\text{new}}(z) \tag{2}$$

where z_{CB} is the cloud base height.

If WRF-Chem is not correctly simulating the amount of precipitation production, an erroneous r_f could be applied in the simulations to produce the correct amount of mixed-phase scavenging. Therefore, in order to evaluate whether r_f values determined by comparing SEs calculated from observations and simulations are accurate, we need to evaluate how well WRF-Chem represents the precipitation production. Models with more detailed representations of microphysical scavenging, such as that in Barth et al. (2001) that tracks gas concentrations in individual hydrometeors, could provide additional information on, for example, the vertical redistribution of gases evaporated from falling precipitation. However, such an approach is very computationally intensive. In the present study we investigate what can be learned from a model widely used for research and forecasting. With the simulated storms put into context with the observations, we use tracers in the WRF-Chem simulations to examine the amounts of entrainment along the storm cores in relation to the background vertical profiles of the trace gases. We then use trajectory output from the inflow region to the storm top from WRF-Chem to determine the relative contributions of scavenging, entrainment, and aqueous chemistry to the trace gas mixing ratios.

This study addresses the following science questions: How well does WRF-Chem simulate the production of hydrometeor types involved in wet removal (affecting our confidence in the r_f values determined from simulations)? How does ice retention affect peroxide and CH_2O removal in an air mass storm and MCS observed during DC3? How much do scavenging, entrainment, and aqueous chemistry contribute to reductions in mixing ratios of peroxides and CH_2O, in particular, the higher than expected CH_3OOH removal? Does contact time (CT) with liquid water vary among storms, and if so, does it affect peroxide and CH_2O outflow mixing ratios via scavenging and/or aqueous chemistry?

2. Methods

2.1. DC3 Case Study Storms

Aircraft and ground-based observations were analyzed and high-resolution simulations (horizontal grid spacing (Δx) = 600 m to 3 km) were performed with WRF-Chem of a severe storm in Oklahoma on 29–30 May 2012, an air mass storm in Alabama on 21 May 2012, and a MCS over Arkansas/Missouri/Illinois/Mississippi on 11–12 June 2012. This study adds to the results from Barth et al. (2016), Fried et al. (2016), and Bela et al. (2016), providing r_f values determined from simulations of the MCS and an analysis of WRF-Chem trajectories that quantifies the contribution of processes (liquid phase scavenging, ice retention, entrainment, and aqueous chemistry) that affect peroxide and CH_2O outflow mixing ratios.

The severe storm (Oklahoma, 29–30 May) triggered ahead of a dryline and cold front, in a prestorm environment with high 0–6-km vertical wind shear (19 m/s) and high Convective Available Potential Energy (CAPE) (3,113 J/kg) (Bela et al., 2016). The 29–30 May storm is considered severe due to the high vertical extents of its cores, some of which penetrated the tropopause that was located at 17 km above sea level (asl, NEXRAD data, not shown), column-maximum radar reflectivities exceeding 60 dBZ (Figures 1 and 2), and maximum updraft velocities exceeding 68 m/s (DiGangi et al., 2016). Furthermore, the storm generated an enhanced

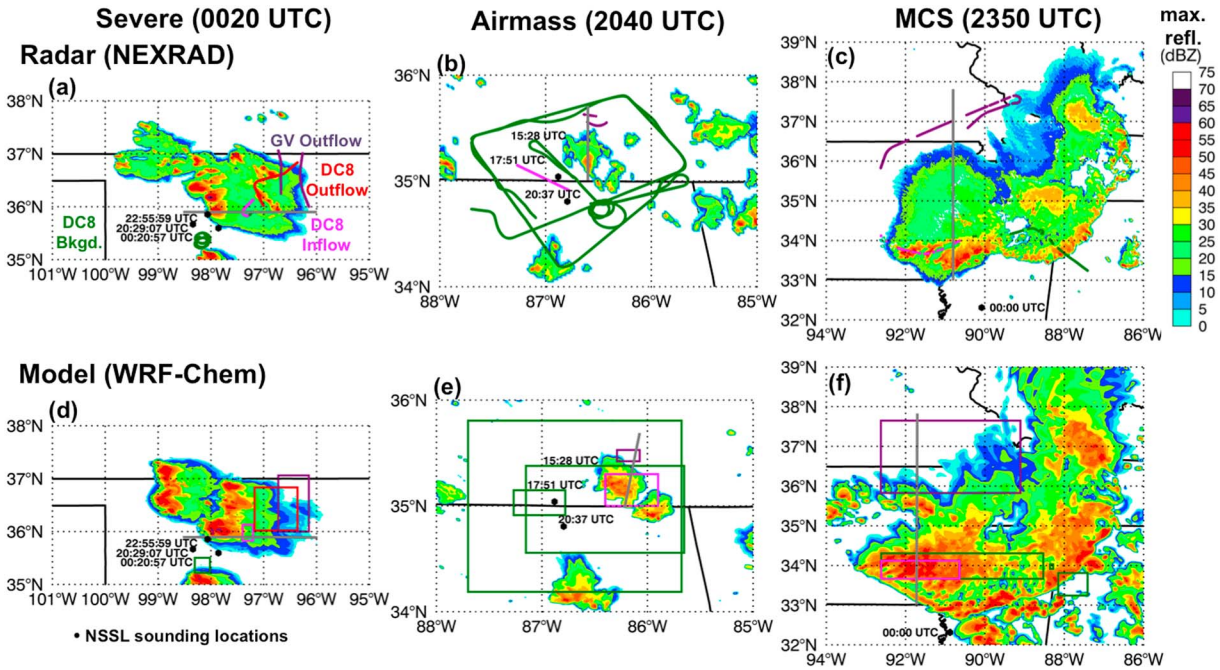

Figure 1. Column-maximum radar reflectivity contours (dBZ) at 00:20 UTC on 29 May 2012 from (a) NEXRAD radar and (d) WRF-Chem simulations, at 20:40 UTC on 21 May 2012 from (b) NEXRAD radar and (e) WRF-Chem simulations, and at 23:50 UTC on 11 June 2012 from (c) NEXRAD radar and (f) WRF-Chem simulations. DC-8 inflow (magenta), GV (purple), and DC-8 (red) outflow, and DC-8 background profile (green) sampling flight segments are shown by lines. The NSSL or UAH sounding locations are indicated by black dots. The gray lines indicate the location of the vertical cross sections depicted in Figure 2. The inflow, outflow, and background profile sampling times and altitudes are listed in Table S1 in the supporting information. NEXRAD = Next-Generation Radar; WRF-Chem = Weather Research and Forecasting model with Chemistry; MCS = mesoscale convective system; NSSL = National Severe Storms Laboratory; UAH = University of Alabama in Huntsville.

Fujita scale 1 (EF1) tornado and large hail (Barth et al., 2015). The southernmost cell had multiple-Doppler coverage for a little over 1 hr (DiGangi et al., 2016).

The discrete ordinary (*air mass*) convective storm (Alabama, 21 May) was initiated by a prefrontal trough and was characterized by low CAPE (~785 Jkg^{-1}) and weak 0–6 km shear (1.54 ms^{-1}). Storm cores attained 12 km altitude and column-maximum reflectivities exceeded 50 dBZ (Figures 1 and 2). It had good coverage by two dual-polarimetric radar (Mecikalski et al., 2015). However, using the i/n-pentane ratio, Fried et al. (2016) determined that aircraft-sampled outflow was significantly more aged than measured inflow, resulting in lower outflow CH_2O values and hence erroneously high SEs, so we did not determine r_f values for this storm. However, analysis of this storm was still useful in comparing various measured parameters with those modeled by WRF-Chem.

The DC-8 aircraft sampled the inflow and the Gulfstream V (GV) aircraft sampled the outflow of an MCS over Missouri and Arkansas from 22 to 23 UTC on 11 June 2012. Numerous moderately vigorous convective updraft cores with reflectivities up to 50 dBZ extending up to altitudes of 17 km were arranged in a bow formation with a trailing anvil (Figures 1 and 2). The National Weather Service sounding at Jackson, Mississippi, at 0 UTC on 12 June 2012 showed high CAPE values (2,668 Jkg^{-1}) and 0–6-km wind shear (13 ms^{-1}). Only NEXRAD data are available for the MCS.

2.2. Aircraft Measurements

Chemistry, aerosol, and cloud physics measurements in inflow, outflow, and the background environment of the three storms were obtained by the National Aeronautics and Space Administration (NASA) DC-8 and the National Science Foundation/National Center for Atmospheric Research (NSF/NCAR) GV. The aircraft instruments are described and the uncertainty parameters of the measurements are given in Bela et al. (2016). Fried et al. (2016) discuss wingtip comparisons of the CH_2O measurements on both airplanes and correct the two instruments to each other in order to calculate CH_2O SEs from the air mass storm and MCS. On the other hand, Barth et al. (2016) note that the instruments used to measure CH_3OOH and H_2O_2 on the DC-8 and GV were not calibrated to each other, and discrepancies were noted in wingtip comparisons. Thus, no peroxide SEs were

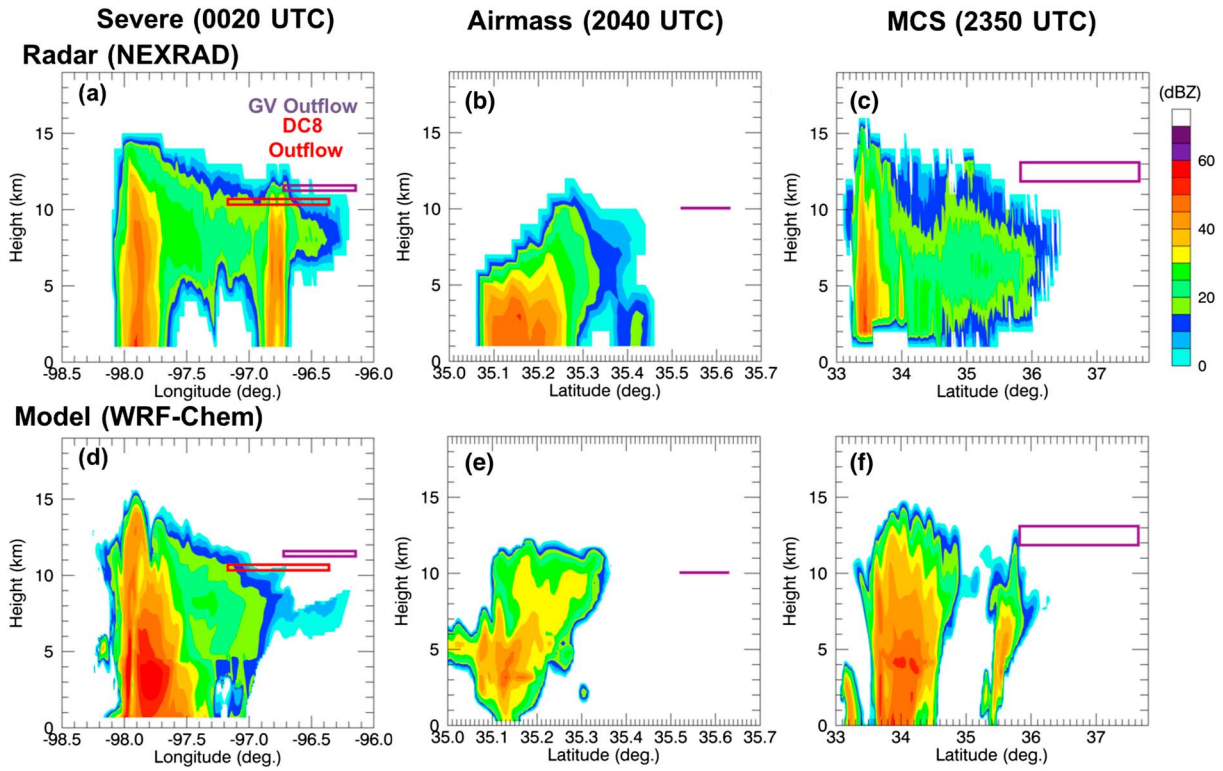

Figure 2. Vertical reflectivity cross sections at the locations shown by the gray lines in Figure 1 at 00:20 UTC on 29 May 2012 from (a) NEXRAD radar and (d) WRF-Chem simulations, at 20:40 UTC on 21 May 2012 from (b) NEXRAD radar and (e) WRF-Chem simulations, and at 23:50 UTC on 11 June 2012 from (c) NEXRAD radar and (f) WRF-Chem simulations. The longitudinal and altitude extents of GV (purple) and DC-8 (red) outflow sampling flight segments are designated by rectangles in both NEXRAD and WRF-Chem panels. NEXRAD = Next-Generation Radar; WRF-Chem = Weather Research and Forecasting model with Chemistry; MCS = mesoscale convective system.

calculated from aircraft measurements by Barth et al. (2016) for the air mass storm and MCS, since for these two storms, inflow was sampled by the DC-8 and outflow measurements were made by the GV. However, we still derive information about peroxide scavenging in these two storms from the WRF-Chem simulations.

2.3. Meteorological Measurements

Radar, precipitation, and sounding data were utilized to compare the dynamical and microphysical properties of the three storms and evaluate these properties in the three storm simulations.

NEXRAD reflectivity (described in Bela et al., 2016) was utilized to delineate storm analysis regions and compute storm 35 dBZ volumes. The simulated precipitation is evaluated with the hourly National Centers for Environmental Prediction (NCEP) Stage IV analysis, a 4-km contiguous U. S. (CONUS) grid mosaic of radar and gauge analyses from the regional River Forecast Centers.

Radiosonde sounding data were used to calculate CTs with liquid water and evaluate simulated wind, temperature, and humidity vertical profiles. Sounding data near the severe storm were collected by the National Severe Storms Laboratory (NSSL) Mobile Global Positioning System Advanced Upper-Air Sounding (MGAUS) system (Ziegler, 2013c), and those in the vicinity of the air mass storm were provided by the University of Alabama in Huntsville (UAH) Mobile Sounding System. For the MCS, the sounding at Jackson, Mississippi, at 0 UTC on 12 June 2012 was used.

Vertical velocity profiles obtained from dual-Doppler radar analyses were used in order to calculate CTs with liquid water and evaluate simulated vertical velocity profiles. The southwesternmost cell of the Oklahoma storm was observed by the NSSL and University of Oklahoma (OU) NO-XP mobile X-band radar and two Shared Mobile Atmospheric Research and Teaching Radars (SMART-R, Biggerstaff et al., 2005, 2017) from about 23 UTC on 29 May 2012 until 0 UTC on 30 May 2012 (DiGangi et al., 2016), with a gridded radar product horizontal (Δx) and vertical (Δz) grid spacing of 500 m. For the air mass storm, dual-Doppler coverage was provided by the KHTX WSR-88D S-band ($\lambda = 10.71$ cm) radar at Hytop, Alabama and the UAH WHNT-TV Advanced

Radar for Meteorological and Operational Research (ARMOR) C-band ($\lambda = 5.5$ cm) radar at the Huntsville International Airport (Mecikalski et al., 2015; $\Delta x = \Delta z = 1$ km). Because dual-Doppler radar observations were not collected for the MCS storm, we used the maximum updraft velocity profile obtained from the convective cores of a small MCS observed during the Thunderstorm Electrification and Lightning Experiment (TELEX, Lund et al., 2009; MacGorman et al., 2008; $\Delta x = \Delta z = 500$ m). The DC3 11–12 June MCS was somewhat larger than the TELEX MCS. At the end of its maturation period, convective cells forming the TELEX MCS extended in a line of about 300 km in extent, while at the end of the aircraft outflow sampling period, the DC3 11–12 June MCS formed a bow shape ~550 km in extent. Nevertheless, the TELEX MCS maximum updraft profile is a reasonable approximation for that in the DC3 11–12 June MCS due to their similar severities. Column-maximum reflectivity attained 55 dBZ in the DC3 11–12 June MCS during the outflow sampling period (Figure 1) and 57.5 dBZ at the mature stage of the TELEX MCS (Lund et al., 2009).

2.4. Model Description and Configuration

2.4.1. Meteorology and Chemistry Configuration

For each storm, four WRF-Chem simulations were conducted in which CH_3OOH, CH_2O, H_2O_2, HNO_3, and SO_2 were scavenged in cloud and raindrops, but retained in snow and graupel/hail with different r_f values ($r_f = 0$, 0.25, 0.5, and 1.0). The WRF-Chem model configurations for the simulations of the three storms are listed in Tables S2–S4 in the SI. An additional simulation with scavenging was conducted with r_f values varying by species, as defined in Leriche et al. (2013) (CH_3OOH and SO_2: $r_f = 0.02$, CH_2O and H_2O_2: $r_f = 0.64$, HNO_3: $r_f = 1$). Leriche et al. (2013) chose the same r_f value for CH_2O as measured in the laboratory for H_2O_2 by von Blohn et al. (2011), due to the relatively similar solubilities of CH_2O and H_2O_2. Finally, a simulation of each storm was conducted with no gas scavenging. Bela et al. (2016) detail the WRF-Chem simulations of the severe storm and the Neu and Prather (2012) (NP2012) wet scavenging scheme used in simulations of all three cases. The NP2012 scheme calculates gas removal due to microphysical scavenging as the product of the temperature-dependent effective Henry's law coefficient (given in the SI of Bela et al., 2016) and the net precipitation formation (conversion of cloud water to precipitation minus evaporation). Additionally, for mixed-phase conditions (258 K $< T <$ 273 K), a constant fraction (r_f = retention factor) of the amount of each species dissolved in cloud water that is converted to newly formed precipitation is returned to the gas phase. The NP2012 scavenging scheme also represents the deposition of gaseous HNO_3 on ice for $T <$ 258 K. Kinetic limitations were not taken into account, which may lead to errors in the liquid phase concentrations of CH_2O and the peroxides. For example, tracers with solubilities similar to those of CH_2O and the peroxides did not attain Henry's Law equilibrium in a 6-s model time step (Barth et al., 2001), and our severe and air mass storm simulations used a 3-s time step. In our simulations, nor are dissolved gases retained in cloud water from one time step or grid cell to the next, as in Barth et al. (2001). The meteorology and chemistry configurations of the air mass storm and MCS simulations are described by Li et al. (2017). In the present study, we add entrainment tracers to the simulations of the air mass storm and MCS and online chemical trajectories to all three simulations.

For the severe storm simulation, the Morrison two-moment microphysics scheme (Morrison et al., 2009) was used, while the air mass storm and MCS simulations utilized the WRF Single-Moment 6-class microphysics (WSM6, Hong & Lim, 2006) parameterization. We have chosen the microphysics scheme for each storm that produces the most realistic simulation, allowing us to examine the effect of different storm dynamics on the importance of mixed-phase versus liquid scavenging. While Salzmann et al. (2007) found some sensitivity in results depending if there were cloud drops in the inflow region of the storm, we did not find this situation in the cases we simulated. We note that in the Morrison scheme for the severe storm simulation, hail-like properties of mixed-phase hydrometeors were chosen (e.g., $\rho_h = 0.9$ g/cm^3), whereas in the WSM6 microphysics parameterization for the air mass storm and MCS simulations, graupel-like mixed-phase hydrometeor characteristics were utilized (e.g., $\rho_g = 0.5$ g/cm^3). Due to its lower density, we would expect the graupel/hail simulated by the WSM6 microphysics scheme to have a larger diameter and thus fall more rapidly than that in the Morrison scheme. Furthermore, the two schemes have different parameterizations of precipitation formation processes, such as the collection of rain by falling ice (Lin et al., 1983; Morrison et al., 2005). The equations used to calculate the net precipitation production for the Morrison scheme are given in the SI of Bela et al. (2016) and for WSM6 microphysics in Text S1 in the SI of this publication.

The three simulations had horizontal grid spacings ranging from 600 m to 3 km and did not use a convective parameterization. With these grid spacings, entrainment may not be produced sufficiently (Bryan et al., 2003; Bryan & Morrison, 2012). Furthermore, statistical convective properties have been shown not to converge

until the grid spacing was reduced to 250 m for an idealized squall line (Lebo & Morrison, 2015). However, computational limitations prevented us from further decreasing the horizontal grid spacing for these simulations.

2.4.2. Tracers

To evaluate whether the simulated amount of entrainment along the storm cores was consistent with that calculated from aircraft hydrocarbon measurements by Fried et al. (2016) (n,i-butane, n,i-pentane, and also n-hexane and n-heptane for the severe storm), we created passive tracers for each 1-km layer of atmosphere from the surface to model top (~20 km for the severe storm simulation and ~19 km for the air mass storm and MCS simulations). The tracers were set to a value of 1.0 in clear air outside of the storms (where $q_c < 0.01$ g/kg) for a single time step approximately 1 hr before the end of the outflow periods (listed in the simulation configuration Tables S2–S4 in the SI). To calculate entrainment from each 1-km altitude layer, the average percent contributions of each 1-km layer were calculated from all model points at the 40-dBZ contour (top of storm core) directly upwind of the aircraft sampling location, within the aircraft outflow sampling altitudes (Barth et al., 2016).

2.4.3. Trajectories

For each storm simulation, 864 online trajectories were initialized in storm inflow regions. The initial locations of the trajectories formed a 3-D grid with eight evenly spaced points in longitude and four points in latitude, and nine points at altitudes of 600–3,000 m (vertical grid spacing (Δz) = 300 m). Trajectories were initiated at these locations at three starting times evenly spaced within the inflow time period. Only trajectories that were ingested by the simulated storms, as determined by having attained the minimum height of the outflow observations, were analyzed. The trajectory initial longitudes and latitudes, longitude and latitude spacings, and start and stop times are given in Table S5 in the SI. For the trajectory analysis, we did not need to assume constant entrainment with altitude because the resulting mixing ratios come from the Eulerian WRF-Chem model which accounts for the 3-D heterogeneity in mixing processes.

3. Evaluation of Meteorology

3.1. Radar Reflectivities

The observed dynamics of the storms were represented well by the model, including locations and times of convective initiation (except for the severe storm, which triggered ~40 min later in simulations than observed), maximum reflectivity in storm cores, anvil height and horizontal extent, and maximum height of the storm cores (Figures 1 and 2). However, the regions of high reflectivity (>35 dBZ) indicative of storm cores were larger in the model simulations than those observed for all three storms, possibly due to a larger volume containing ice in the simulations than observed and/or differences in the effective reflectivity calculation between the radar and WRF-Chem. Bela et al. (2016) and Li et al. (2017) provide a detailed evaluation of the WRF-Chem meteorology with radar observations.

3.2. Entrainment

The average amount of entrainment per kilometer (%km^{-1}) from WRF-Chem (Figure 3) compares well with Fried et al. (2016) who used hydrocarbon trace gases (severe storm, WRF-Chem: 7.8 ± 5.4%km^{-1}, Fried et al. (2016): 7.6 ± 1.0%km^{-1}; air mass storm, WRF-Chem: 10 ± 9.2%km^{-1}, Fried et al. (2016): 8.94 ± 2.7%km^{-1}). However, the mean amount of entrainment calculated from WRF-Chem tracers for the MCS (7.3 ± 6.5%km^{-1}) is nearly twice as high as that calculated by Fried et al. (2016; 4.4 ± 1.0%km^{-1}). For the MCS, we note that the background hydrocarbon profiles used by Fried et al. (2016) were calculated from all clear-air measurements for the entire DC-8 flight, spanning a large geographic area from Kansas to Arkansas, and not necessarily representing the air entrained directly into the MCS. Although this discrepancy in entrainment rate needs further investigation, as we will show later, the average SE determined by Fried et al. (2016) and the WRF-Chem simulations here are in close agreement for the MCS.

3.3. Storm Properties

To learn how much confidence to place in the r_f values determined in this study, we compare observed and simulated maximum vertical velocities, 35 dBZ volumes, hail volumes retrieved from dual-polarimetric radar, hydrometeor fields, and surface precipitation. All of these properties are affected by and provide information about the precipitation production rates in the storm cores, which were not measured.

Observed and simulated storm parameters and precipitation totals were calculated starting at the model output time (10-min output interval) closest to the beginning of the inflow period through the model output time closest to the end of the outflow period. For calculations of storm parameters, spatial masks were

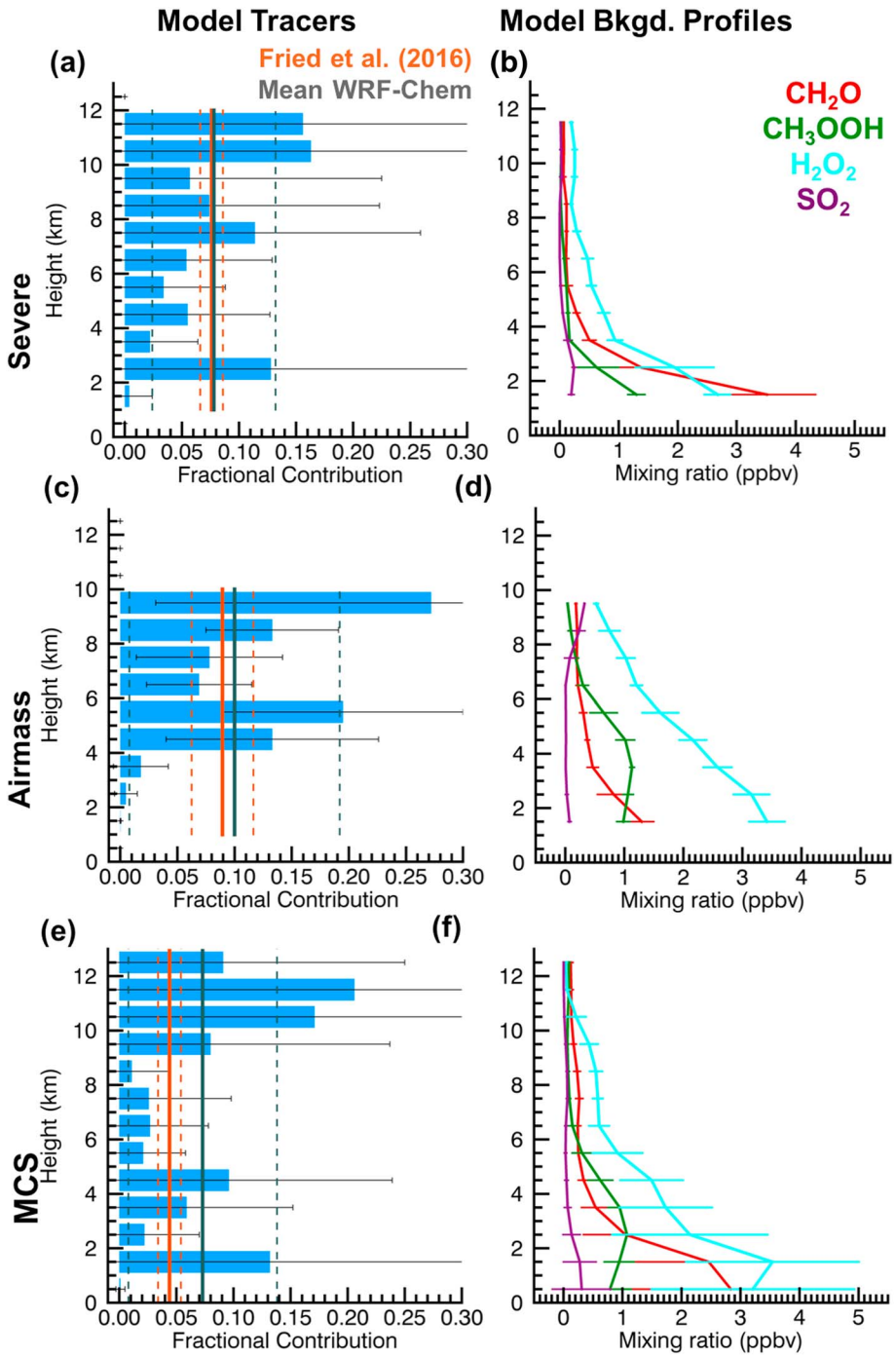

Figure 3. Fractional contributions of air from 1-km vertical levels calculated from WRF-Chem tracers, background profiles of soluble trace gases calculated from WRF-Chem simulations for (a, b) severe storm, (c, d) air mass storm, and (e, f) MCS, respectively. The numerical fractional contribution values are given in Table S6 in the SI. WRF-Chem = Weather Research and Forecasting model with Chemistry; MCS = mesoscale convective system.

created based on the column-maximum reflectivity fields from NEXRAD and WRF-Chem or on the surface precipitation rates. For the severe storm, the spatial masks were restricted to the southeasternmost convective cell (Kingfisher storm) to facilitate comparison with the radar analyses. For the MCS, the masks were limited to the western portion of the MCS where convective cores lay between the flight tracks of the inflow and outflow observations. No spatial masks were required for the air mass storm as it covered a small area

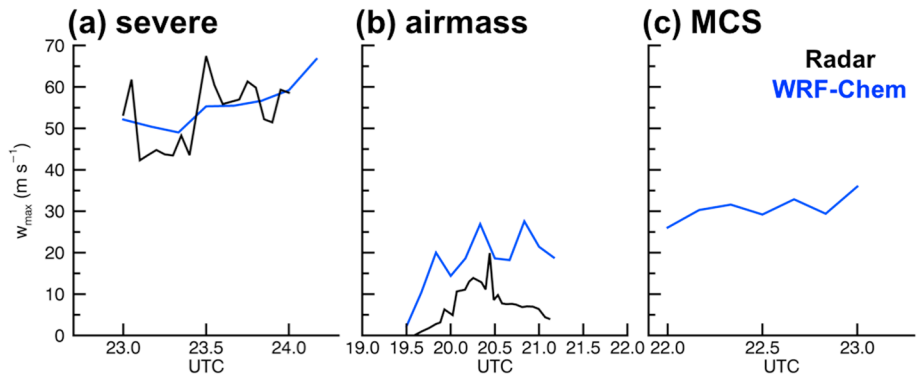

Figure 4. Maximum updraft velocities (ms^{-1}) calculated from radar (black lines) and WRF-Chem (blue lines) for the (a) severe storm, (b) air mass storm, and (c) MCS. WRF-Chem = Weather Research and Forecasting model with Chemistry; MCS = mesoscale convective system.

and was completely sampled by the radar. The spatial masks for the surface precipitation fields are depicted in Figure S5 in the (SI).

3.3.1. Vertical Velocity

Maximum vertical velocity (w_{max}) time series were determined from dual-Doppler radar analyses for the severe and air mass storms and from the WRF-Chem output for all three storms (Figure 4). For the severe storm, the maximum updraft velocity simulated by WRF-Chem shows relatively good agreement with that retrieved from radar. There is in the radar w_{max} (45 to 65 ms^{-1}) compared to the WRF-Chem w_{max} (50 to 65 ms^{-1}), which may be related to the smoothing effect of the coarser horizontal grid resolution in WRF-Chem ($\Delta x = 1$ km, effective horizontal grid resolution ~5–7 km due to model numerics (Skamarock, 2004)) versus the radar ($\Delta x = 500$ m). On the other hand, for the air mass storm, simulated maximum updraft velocity is up to 4 times higher than that retrieved from radar (at 20:50 UTC, observed: 5 ms^{-1}; simulated: 20 ms^{-1}), particularly from 20:30 UTC to 21:20 UTC. The simulated overestimate in updraft velocities is despite the coarser effective resolution in WRF-Chem ($\Delta x = 600$ km, effective horizontal grid resolution ~3–4 km) versus the radar ($\Delta x = 1$ km). For the severe and air mass storm radar velocity analyses, DiGangi et al. (2016) and Mecikalski et al. (2015) used variational methods to integrate the mass continuity equation. Potvin et al. (2012) found relative root-mean-square errors in updraft velocity retrieved using variational methods ranging from 45% to 90%, depending on the radar scan method and larger at higher altitudes. Mecikalski et al. (2015) suggested that their retrieved velocities may be underestimated due to integration errors and the 1-km grid spacing.

3.3.2. Hydrometeor Fields

Time series of 35-dBZ volumes (Figure 5) were computed from NEXRAD radar and WRF-Chem simulations within the spatial masks. Hail volumes for the air mass storm (Figure 5) were obtained from output from the NCAR particle identification (PID) package (Mecikalski et al., 2015). The grouping of the 17 PID classifications into the five WSM6 microphysics classes is given in Table S7 in the SI. The WRF-Chem 35 dBZ volumes are much greater than those calculated from NEXRAD for the entire period for the severe storm (up to more than 2 times larger) and the MCS (up to 7 times larger). For the air mass storm, while the simulations reproduce well the observed 35 dBZ and hail volumes from 19:30 to 20:20 UTC, the simulated 35 dBZ and hail volumes then increase rapidly to more than 5 times larger and 18 times larger than observed, respectively, by 21:20 UTC. The air mass storm and MCS simulations overestimate graupel/hail volume much more than the severe storm simulation, which may be due in part to the use of different microphysics schemes. Due to its lower density, we expect the graupel/hail simulated by the WSM6 microphysics scheme to potentially remain for shorter periods of time within the storms than the graupel/hail simulated by the WSM6 microphysics scheme.

For the severe storm, WRF-Chem hydrometeor mass concentrations (mass per volume) are compared with those from the Diabatic Lagrangian Analysis (DLA) model (Ziegler, 2013a, 2013b; see methods in Text S2 of the SI). Although the DLA is also a microphysical model (Lagrangian versus the Eulerian WRF-Chem), it uses wind and reflectivity fields from dual-Doppler radar analyses and an environmental sounding as input, and thus avoids some of the uncertainties associated with the simulated dynamical and microphysical processes.

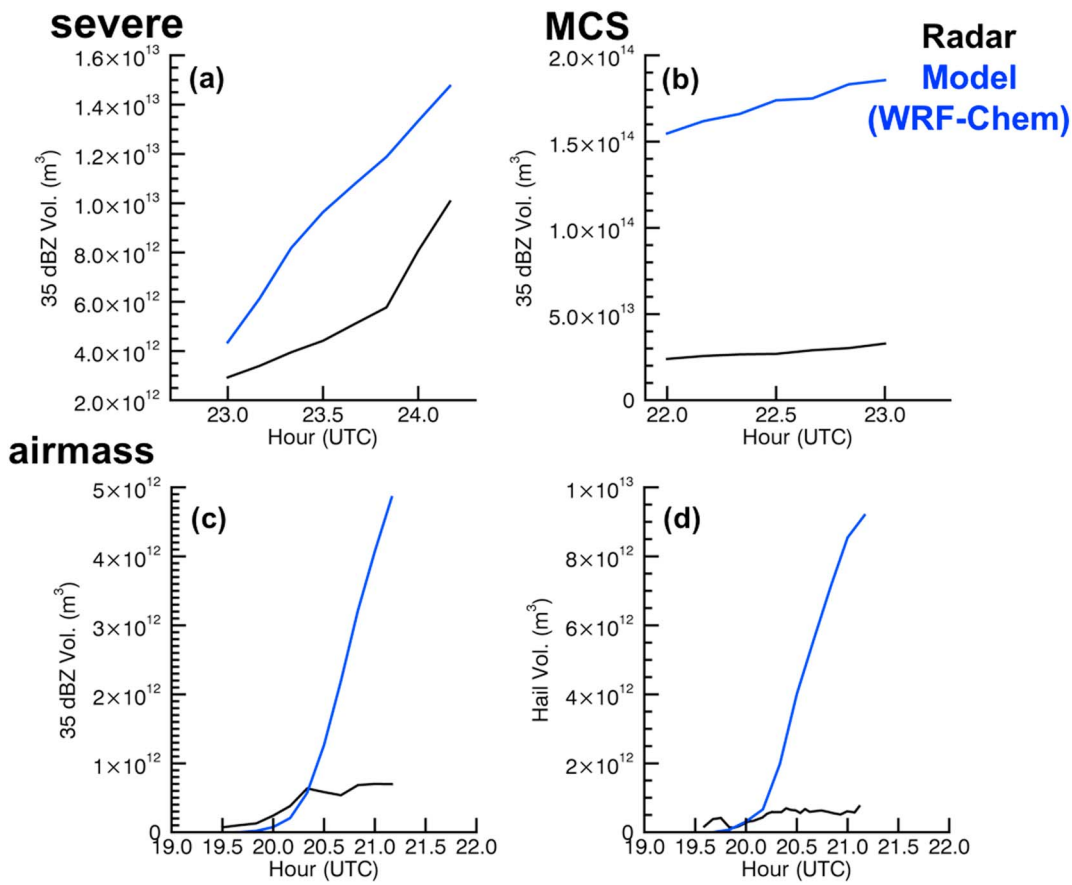

Figure 5. The 35-dBZ volumes (m^3) calculated from radar (black) and WRF-Chem (blue) for (a) severe storm, (b) MCS, (c) air mass storm, and (d) hail volume (m^3) from dual-polarimetric radar (black) and WRF-Chem (blue) for the air mass storm. WRF-Chem = Weather Research and Forecasting model with Chemistry; MCS = mesoscale convective system.

Nevertheless, uncertainty in the DLA hydrometeor fields comes from errors in the radar-retrieved wind fields and the calculation of model reflectivities using simplified backscatter models and parameterized size/shape distributions (Ziegler, 2013b).

In the WRF-Chem severe storm simulation, areas of column-maximum reflectivity >35 dBZ are somewhat larger than those retrieved from the polarimetric radar (Figure S6 in the SI), as noted for the comparison of WRF-Chem with NEXRAD for all three storms (Figure 1).

For the severe storm comparison of WRF-Chem and DLA simulations, we are interested in evaluating the simulated hydrometeor mass concentrations in temperature ranges relevant for microphysical scavenging of the peroxides and CH_2O (cloud water between cloud base and 0°C and 0°C and −15°C, rain between cloud base and 0°C, cloud ice between cloud base and 0°C and 0°C and −15°C, and graupel/hail and snow between 0°C and −15°C). Based on the time series of hydrometeor concentrations (Figure 6), severe storm cloud water concentrations are underpredicted and rain and hail are overpredicted by WRF-Chem compared to the DLA results. Thus, WRF-Chem is potentially converting too much cloud water to rain and hail, so that true r_f values may be higher than what we find in this study using WRF-Chem.

We note that the DLA severe storm simulation assumes a variable bulk graupel/hail density that varies with height for mixed-phase precipitation ($\rho_h = 0.63$ to 0.69 gcm^{-3}) versus the higher solid ice density assumed in the WRF-Chem simulations of the severe storm ($\rho_h = 0.9$ gcm^{-3}). Thus, the DLA graupel/hail is likely to have larger particle diameters and thus fall more rapidly, and therefore would experience a lower riming rate given comparable particle size distributions. Indeed, the highest mass concentrations of graupel/hail in DLA are at lower altitudes (2–5 km asl) than the peak graupel/hail mass concentrations in WRF-Chem (5–15 km asl; Figure S9 in the SI).

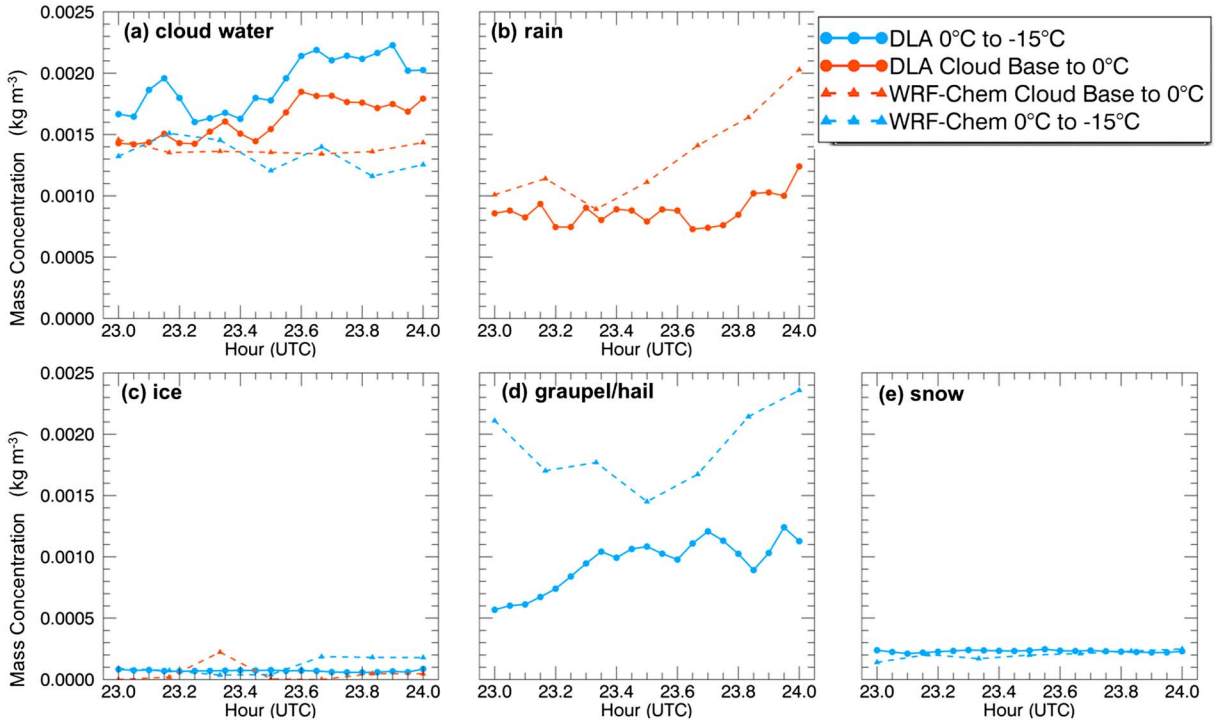

Figure 6. Mass concentration (kgm^{-3}) of (a) cloud water, (b) rain, (c) cloud ice, (d) graupel/hail, and (e) snow for $w > 3$ m/s regions integrated from cloud base to 0°C (orange-red), and 0°C to −15°C (light blue) from radar/DLA analysis (dots and solid lines) and WRF-Chem simulations (triangles and dashed lines) for the severe storm. For each hydrometeor type, only the mass concentrations integrated for temperature ranges in which the hydrometeor contributes to gas scavenging in the WRF-Chem simulations are shown. DLA = Diabatic Lagrangian Analysis; WRF-Chem = Weather Research and Forecasting model with Chemistry.

3.3.3. Surface Precipitation

The total precipitation volume (Table 1) for the severe storm for the analyzed hour is more than twice as high in the simulations as in the NCEP Stage IV data. However, the precipitation is spread out over a larger surface area in the simulations (Figure S5 in the SI), so that the mean hourly surface precipitation rate is one half in the simulations than in the NCEP Stage IV data. Furthermore, the maximum hourly surface precipitation rate simulated by WRF-Chem is 40% lower than observed.

For the air mass storm, the total surface precipitation volume over the analyzed 3-hr period is about 14% less in the simulations than in the NCEP Stage IV data. The mean hourly surface precipitation rate is 15% higher in the simulations than in the NCEP Stage IV data, and the maximum precipitation rate is 20% higher simulated by WRF-Chem than observed. Although the total surface precipitation volume for the MCS is twice as high in simulations than in observations, the mean hourly surface precipitation rate is only 15% higher in the simulations than in the NCEP Stage IV data, and the maximum hourly surface precipitation rate is only 20% higher simulated by WRF-Chem than observed. Thus, the simulations of the air mass storm and MCS reasonably reproduce the observed surface precipitation rate, and thus potentially the 3-D precipitation production rate, while for the severe storm the mean hourly surface precipitation rate is underestimated

Table 1
Precipitation Volumes (m^3) and Mean and Maximum Precipitation Rates (mmhr^{-1}) from NCEP Stage IV Data and WRF-Chem Simulations

		Total (m^3)		Mean rate (mmhr^{-1})		Maximum rate (mmhr^{-1})	
Storm	Time (UTC)	Obs.	WRF-Chem	Obs	WRF-Chem	Obs	WRF-Chem
Severe	23–00	8.60×10^6	2.66×10^7	11.7	5.7	42	23
Air mass	19–22	1.69×10^7	1.45×10^7	2.3	2.6	30	34
MCS	22–23	1.56×10^8	4.19×10^8	4.9	5.5	39	46

Note. The mean hourly surface precipitation fields for each storm are depicted in Figure S5 in the SI.

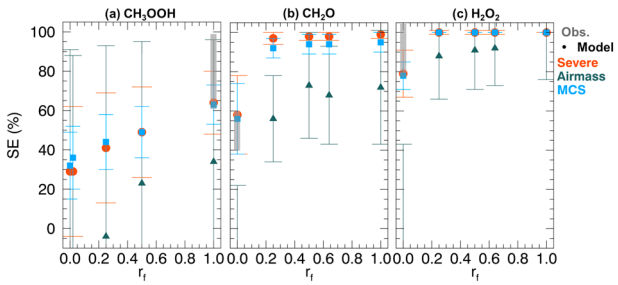

Figure 7. SEs of (a) CH_3OOH, (b) CH_2O, and (c) H_2O_2 calculated from WRF-Chem simulations (dots) for different r_f values for severe (orange red) and air mass (dark gray) storms and MCS (blue). The r_f values for which SEs calculated from WRF-Chem agree with those determined from aircraft observations (Barth et al., 2016; Fried et al., 2016) are shaded in gray. SE = scavenging efficiency; WRF-Chem = Weather Research and Forecasting model with Chemistry; MCS = mesoscale convective system.

in the simulations relative to observations. If the overestimate in the surface precipitation rate indicates that the simulated precipitation production rate inside the storm is too high, the true r_f values would be higher than those found in this study from the WRF-Chem simulations.

4. Ice Retention Fractions Determined Using Simulations and Observations

Values of r_f were determined by identifying the WRF-Chem simulation for which SEs calculated from simulations agree with those calculated from observations. This method assumes that the model is correctly simulating all other parameters in equation (5) (effective Henry's Law coefficient, gas phase mixing ratio, precipitation production rate), so that the r_f value chosen in the simulation will determine the amount of scavenging. SEs were calculated from the WRF-Chem simulations as the percentage difference in mean outflow values between a simulation with scavenging and the simulation without scavenging:

$$\mathrm{SE}(\%) = 100 \times \left(\frac{q_{i,\mathrm{noscav}} - q_{i,\mathrm{scav}}}{q_{i,\mathrm{noscav}}} \right) \tag{3}$$

where $q_{i,\mathrm{noscav}}$ and $q_{i,\mathrm{scav}}$ are the mean outflow mixing ratios of species i in the simulation without wet scavenging and a simulation with wet scavenging, respectively. Mean outflow values are calculated from the model latitude-longitude regions depicted in Figures 1d–1f and the altitude ranges sampled by the aircraft (Table S1 in the SI), and $q_c > 0.01$ gkg^{-1}. The error analysis is given in Text S3 of the SI. Values of SEs calculated from aircraft observations were determined by Barth et al. (2016) and Fried et al. (2016) using an altitude-dependent entrainment model based on inflow and background mixing ratios and a mean entrainment rate determined from hydrocarbon measurements.

The SEs of CH_3OOH, CH_2O, and H_2O_2 calculated from WRF-Chem simulations using different r_f values and the SE ranges calculated from aircraft observations (77 ± 20% for CH_3OOH and 88 ± 11% for H_2O_2, severe storm only, Barth et al., 2016; 54 ± 5% and 48 ± 7% for CH_2O for the severe storm and MCS, respectively, Fried et al., 2016) are depicted in Figure 7. We note that the severe storm and MCS simulations use different microphysics schemes (necessary to produce the best simulation of the storm timing, location, size, and intensity), and thus may have different vertical distributions of precipitation production rates. The scavenging scheme in WRF-Chem calculates microphysical removal based on the precipitation production and the temperature range, so that the vertical distribution of precipitation production could affect the amount of scavenging. Nevertheless, we see similar vertical profiles of net precipitation production in the online WRF-Chem trajectories (Figure 8) among the three storm simulations. We did not determine ice retention coefficients from the air mass storm because Fried et al. (2016) showed that the aircraft-sampled inflow and outflow air masses were not related. In addition, the error bars of the SEs calculated from the WRF-Chem simulations of the air mass storm are quite large due to high variability of simulated outflow mixing ratios (Table S9 in the SI), possibly due to large amounts of entrainment in the storm anvil or temporal variability in updraft microphysics or thermodynamics.

The r_f for CH_2O in the MCS is <0.25 (Figure 7), in agreement with the results in Bela et al. (2016) for the severe storm. Using the CH_2O SE calculated by Fried et al. (2016) using the n-butane ratio method (67 ± 20%), to avoid potential errors from using a horizontally averaged background profile in the altitude-dependent calculation, we still find $r_f < 0.25$ for CH_2O. These results conflict with the laboratory measurements of $r_f = 0.97$ for CH_2O (Jost et al., 2017). Nevertheless, for the severe storm and MCS, the analysis in the previous section indicates that the simulations are overestimating precipitation production, and thus, the true r_f values may be higher. We also note that the SEs calculated from WRF-Chem simulations used mean outflow values. On the other hand, Fried et al. (2016) extrapolated CH_2O mixing ratios from the anvil aircraft sampling location to the top of the storm core to remove the decrease of CH_2O with distance from the storm core due to mixing and photochemistry (photolysis and reaction with OH) and also accounted for CH_2O production from isoprene and loss by photolysis and reaction with OH in the storm core. Thus, the mean CH_2O outflow mixing ratio used to calculate the MCS SE was higher in Fried et al. (2016) (1.52 ppbv) than in this study (1.01 ppbv),

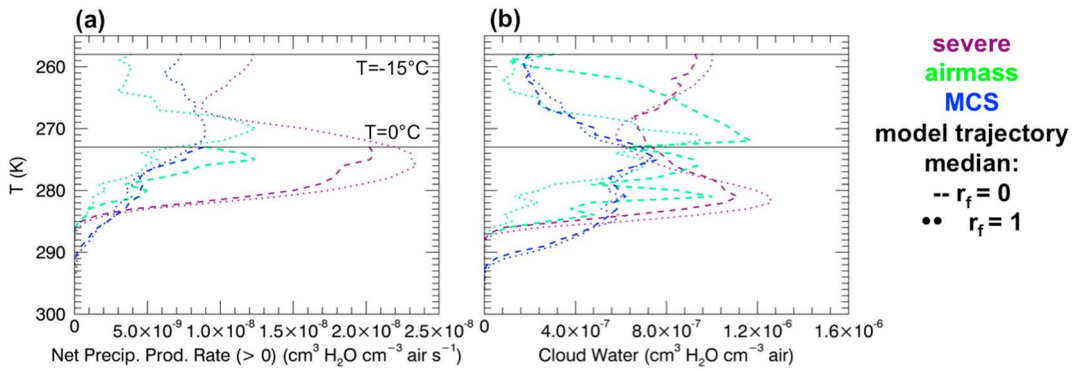

Figure 8. Vertical profiles from WRF-Chem online trajectories of the (a) net precipitation production rates (precipitation minus evaporation, $cm^3\ H_2O \cdot (cm\ air)^{-3} \cdot s^{-1}$) and (b) cloud water mass mixing ratios ($cm^3\ H_2O(cm\ air)^{-3}$). WRF-Chem = Weather Research and Forecasting model with Chemistry; MCS = mesoscale convective system.

resulting in a lower SE determined by Fried et al. (2016). Still, the MCS CH_2O SE calculated using mean outflow aircraft observations and the altitude-dependent method (64 ± 14%) is similar to that from the n-butane method and close to the average SE of 58 ± 13% determined by Fried et al. (2016) for the MCS employing the altitude-dependent and n-butane methods. Furthermore, WRF-Chem SEs calculated using mean mixing ratios at the top of storm core (40 dBZ contour) did not alter the r_f results (Barth et al., 2016; Fried et al., 2016).

Although we do not have SEs calculated from observations for the peroxides, we can still use the simulations to provide information about the role of ice retention in peroxide removal. The simulated CH_3OOH SE is highly sensitive to the r_f value for all three storms (Figure 7), suggesting that ice retention is a major process affecting the amount of CH_3OOH removal. On the other hand, CH_2O and H_2O_2 SEs are relatively insensitive to the r_f value, especially for the severe storm and MCS, for which simulated SEs for $r_f \geq 0.25$ are greater than 90% for CH_2O and H_2O_2 and equal to 100% for H_2O_2 (Figure 7), much higher than the SEs calculated from observations. The larger error bars for the SEs calculated from the model for CH_3OOH than for CH_2O and H_2O_2 are due to higher variability in the simulated outflow mixing ratios (Table S9 in the SI). The differing r_f sensitivities suggest that mixed-phase scavenging has a minor impact on CH_2O and H_2O_2 outflow mixing ratios, because sufficient removal of CH_2O and H_2O_2 occurs even with no ice retention. However, as shown in the previous section, the true r_f values may be higher since rain and hail are overpredicted in the severe storm simulation. On the other hand, rain production is likely to be reasonably simulated for the air mass storm and MCS, yet CH_2O and H_2O_2 scavenging are little affected by r_f for those two storms. In section 5, we analyze the specific processes responsible for these r_f results.

We also calculated SEs for the three storms for HNO_3 (41%–54%) and SO_2 (85%–95%, Table S10 in the SI), but due to the large uncertainties in HNO_3 and SO_2 measurements, HNO_3 and SO_2 scavenging is not analyzed in detail in this paper. Simulated HNO_3 SEs (13%–39%, Table S10 in the SI) are not sensitive to r_f, suggesting liquid phase scavenging and direct deposition to ice dominate HNO_3 removal. Simulated SO_2 SEs are sensitive to r_f for the severe storm (SE = 38%–94% for $r_f = 0$–1) and MCS (SE = 53%–97%), but not for the air mass storm (17%–27%), indicating that ice retention may also be an important removal process for SO_2. The r_f values from the MCS WRF-Chem simulations with SEs that agree with those calculated from observations for HNO_3 and SO_2 are given in Table S11 in the SI.

Observed CH_3OOH SEs are greater than expected from previous field measurements (Cohan et al., 1999) and from its moderate solubility (H_{eff} at 12°C = 694 $Matm^{-1}$). For the severe storm, the SE for CH_3OOH (77%) is higher than that for CH_2O (54%), although the effective Henry's Law coefficient is higher for CH_2O (includes formation of $CH_2(OH)_2$, H_{eff} at 12°C = 9,580 $Matm^{-1}$). In addition, the CH_3OOH severe storm SE is nearly as high as the H_2O_2 SE (88%), although H_2O_2 is much more soluble (H_{eff} at 12°C = 258,000 $Matm^{-1}$) than CH_3OOH. In the next section, we examine possible reasons for the higher than expected CH_3OOH SEs, such as sinks related to aqueous phase chemistry or entrainment.

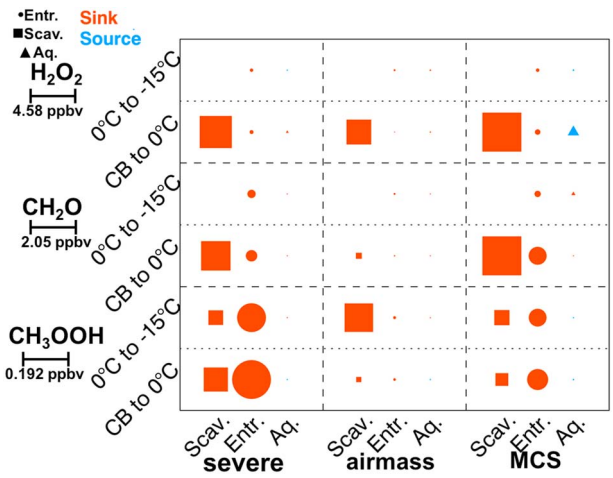

Figure 9. Median changes in −15°C mixing ratios (ΔA, ppbv) due to entrainment (dots), scavenging (squares), and aqueous chemistry (triangles) calculated from WRF-Chem trajectories (entrainment: simulation without scavenging; scavenging and aqueous chemistry: simulations with scavenging and $r_f = 0$ for CH_2O and H_2O_2 and $r_f = 1$ for CH_3OOH). Net sinks ($\Delta A_{-15°C} < 0$) are depicted in red and net sources ($\Delta A_{-15°C} > 0$) in blue. The numerical values are given in Tables S14–16 the supporting information. WRF-Chem = Weather Research and Forecasting model with Chemistry; MCS = mesoscale convective system.

5. Trajectory Analysis of Processes Potentially Affecting SEs

5.1. Scavenging, Entrainment, and Aqueous Chemistry

We compare the microphysical scavenging, entrainment, and aqueous chemistry sources and sinks of CH_2O and the peroxides by calculating the changes in mixing ratios at the top of the mixed-phase region (defined in the model as −15°C) due to processes occurring from cloud base to −15°C ($\Delta MR_{t=CB\ to-15°C}$, equations in Text S4 in the SI) for online WRF-Chem trajectories that pass through the storm cores. Calculating the changes in mixing ratios at the top of the scavenging regions allows us to compare the effects of different processes on outflow mixing ratios among the three storms. We analyzed trajectories from the simulations with $r_f = 1$ for CH_3OOH and $r_f = 0$ for H_2O_2 and CH_2O, as these r_f values provide the best agreement with SEs calculated from observations.

In the simulations without scavenging, if no simulated change in species mixing ratios occurs due to gas phase chemistry, the change in mixing ratio from one time step to the next is due solely to mixing. Photochemistry can also produce or destroy CH_2O, but Fried et al. (2016) estimate a maximum change in CH_2O SEs due to gas phase chemistry of 3%. The maximum change in SEs occurred for the 11–12 June MCS case, where high PBL isoprene levels led to a net production of CH_2O. Barth et al. (2016) found little impact of gas phase chemistry on CH_3OOH and H_2O_2 outflow mixing ratios.

Microphysical scavenging is the dominant removal process for CH_2O ($\Delta MR_{t=CB\ to-15°C} = -0.27$ to -2.1 ppbv, Figure 9) and H_2O_2 ($\Delta MR_{t=CB\ to-15°C} = -2.9$ to -4.6 ppbv) in all three storms and for CH_3OOH ($\Delta MR_{t=CB\ to-15°C}$=−0.15 ppbv) in the air mass storm. On the other hand, depletion by entrainment is the dominant process reducing CH_3OOH mixing ratios ($\Delta MR_{t=CB\ to-15°C}$=−0.21 to 0.36 ppbv) in the severe and MCS storms. In the MCS, aqueous chemistry is the second most important process and a net source for H_2O_2 ($\Delta MR_{t=CB\ to-15°C} = 1.4$ ppbv). Otherwise, aqueous chemistry has the least impact of the three processes on the changes in CH_3OOH, CH_2O, and H_2O_2 mixing ratios from cloud base to the −15°C level ($\Delta MR_{t=CB\ to-15°C} = -0.21$ to 0.0017 ppbv).

Vertical profiles of concentrations of CH_3OOH, CH_2O, and H_2O_2 and changes in number of moles of CH_3OOH, CH_2O, and H_2O_2 due to scavenging, entrainment, and aqueous chemistry, normalized to account for the different grid cell volumes and time steps in the simulations of the three storms (Figure 10), show that CH_2O and H_2O_2 are nearly completely removed for $T > 0$°C by precipitation scavenging. Thus, due to the higher solubilities of CH_2O and H_2O_2 than CH_3OOH, no retention in ice is needed to remove additional gas between 0°C and −15°C, as is the case for CH_3OOH, especially for the air mass storm. More peak scavenging, located near the freezing level, of all three species occurs for the severe storm than for the air mass storm and MCS, likely due to the higher peak precipitation production rate in the severe storm [2.3×10^{-8} (cm $H_2O)^3 \cdot$ (cm air)$^{-3} \cdot s^{-1}$, Figure 8] than air mass storm [1.2×10^{-8} (cm $H_2O)^3 \cdot$ (cm air)$^{-3} \cdot s^{-1}$] and MCS [8×10^{-9} (cm $H_2O)^3 \cdot$ (cm air)$^{-3} \cdot s^{-1}$].

At a given level in a storm core, the change in the mixing ratio of a gas due to entrainment is the product of the background mixing ratio of the gas (Figure 3) and the amount of entrainment. The higher amount of maximum depletion due to entrainment in the air mass storm relative to the severe storm and MCS is due to both higher entrainment percentages from ~5–10 km asl (Figure 3) and higher simulated mixing ratios of CH_3OOH and H_2O_2 (Figure 3) from ~3–9 km asl in the air mass storm than in the severe storm and MCS. The increases in CH_3OOH mixing ratio at ~14°C for the severe storm and ~0°C for the air mass storm (Figure 10) are due to entrainment of background air.

Aqueous chemistry has a minor effect on CH_3OOH, with net depletion rates 3 to 10 times smaller than entrainment and scavenging of CH_3OOH. The highest aqueous chemistry depletion rate of CH_2O and H_2O_2 occurs in the severe storm at $T > 0$°C, likely because of the higher peak cloud water mixing ratios in the severe storm [1.3×10^{-6} (cm $H_2O)^3$(cm air)$^{-3}$, Figure 8] and air mass storm [1.2×10^{-6} (cm $H_2O)^3$(cm air)$^{-3}$) than MCS [7×10^{-7} (cm $H_2O)^3$ (cm air)$^{-3}$].

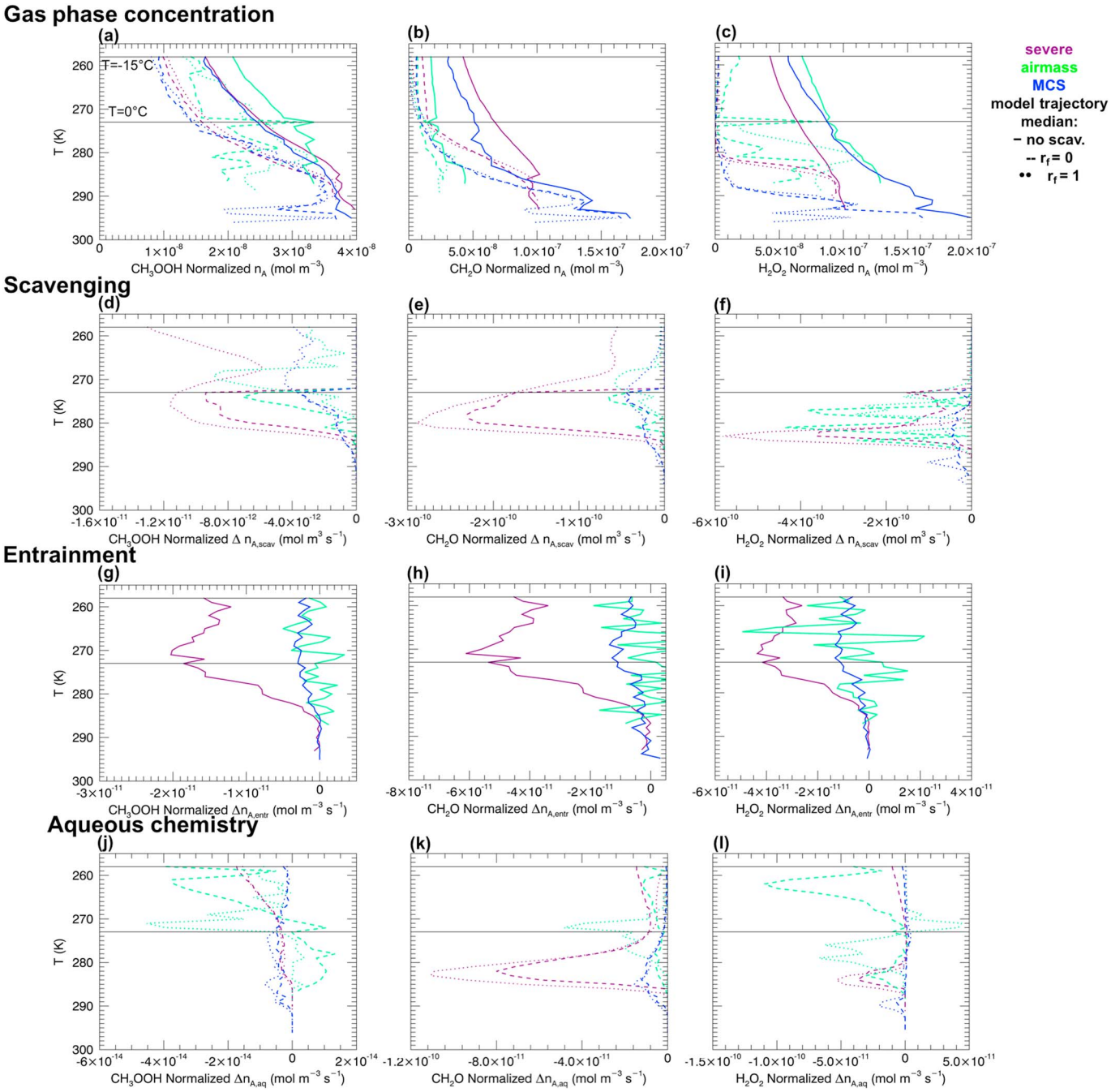

Figure 10. Vertical profiles from WRF-Chem online trajectories of the normalized number of moles (molm^{-3}) of (a) CH_3OOH, (b) CH_2O, and (c) H_2O_2; normalized changes in number of moles due to scavenging (mol · m^{-3} · s^{-1}) of (d) CH_3OOH, (e) CH_2O, and (f) H_2O_2; normalized changes in number of moles (mol · m^{-3} · s^{-1}) due to entrainment of (g) CH_3OOH, (h) CH_2O, and (i) H_2O_2, and normalized changes in number of moles due to aqueous chemistry (mol · m^{-3} · s^{-1}) of (j) CH_3OOH, (k) CH_2O, and (l) H_2O_2. Profiles from WRF-Chem simulations without scavenging are depicted with solid lines, $r_f = 0$ simulations with dashed lines, and $r_f = 1$ simulations with dotted lines. WRF-Chem = Weather Research and Forecasting model with Chemistry; MCS = mesoscale convective system.

Summarizing the findings of the trajectory analysis, in the severe storm and MCS, more CH_3OOH is removed than expected primarily due to depletion by entrainment. On the other hand, lower CH_3OOH and H_2O_2 SEs in the air mass storm than in the severe storm or MCS are partly due to more replenishment by entrainment. Furthermore, ice retention is responsible for a significant portion of reductions in CH_3OOH mixing ratios. Finally, aqueous chemistry does not have a significant impact on outflow mixing ratios of all three species. Therefore, the trajectory analysis shows that it is reasonable to not include aqueous chemistry reactions affecting

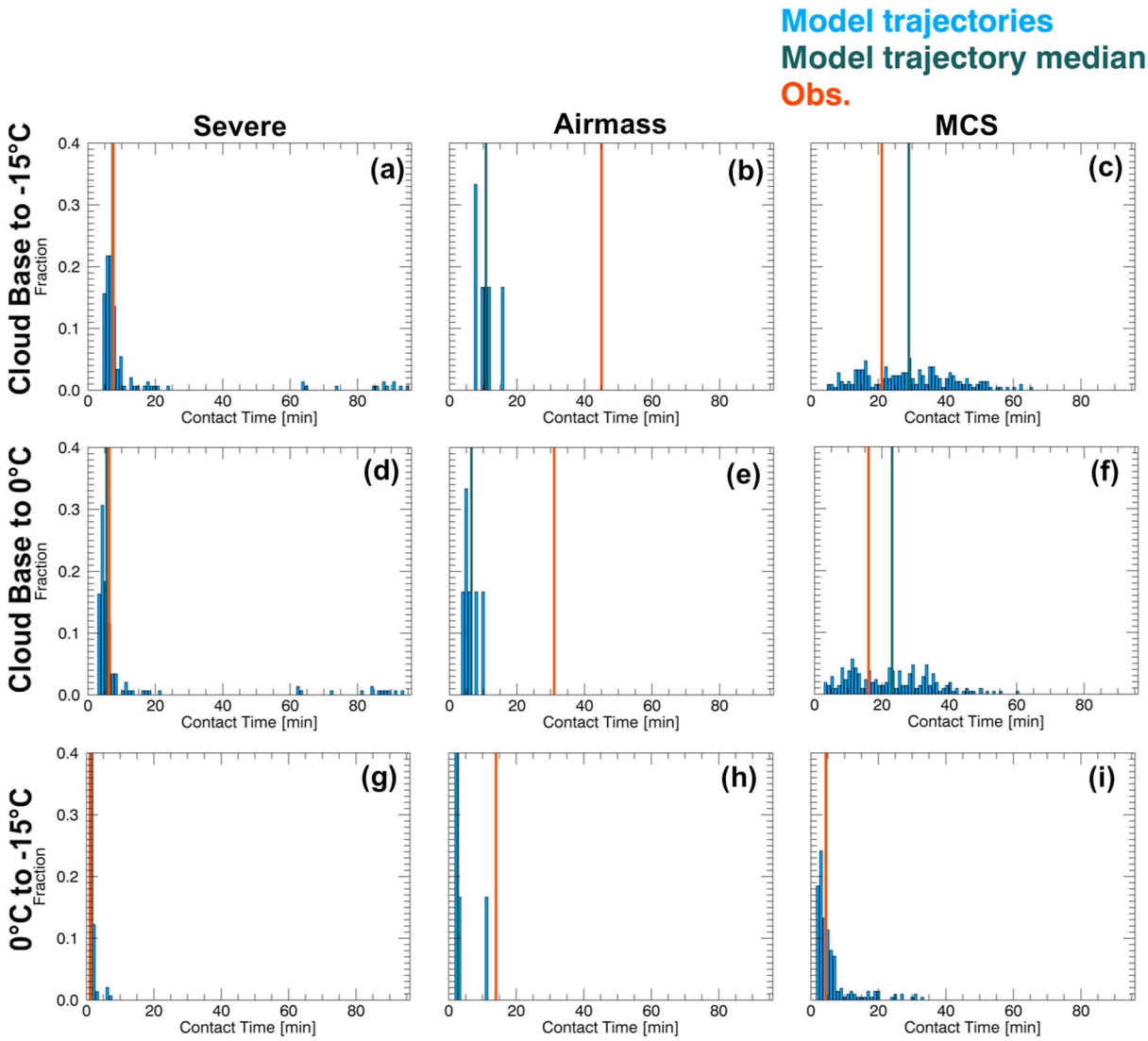

Figure 11. Histograms of simulated CTs (min) with liquid water from WRF-Chem trajectories for (a–c) cloud base to −15°C, (d–f) cloud base to 0°C, and (g–i) 0°C to −15°C for severe and air mass storms and MCS, respectively. The median simulated CTs and those calculated from observations are depicted by gray and red lines, respectively. Observed and simulated CTs, maximum updraft velocities, and cloud base, 0°C, and −15°C heights and the depths between them are listed in Table S17 in the SI. Where only the red line appears, median values from simulations and observations agree. WRF-Chem = Weather Research and Forecasting model with Chemistry; MCS = mesoscale convective system.

these three species (e.g., to reduce computational cost). Thus, future research efforts should be focused on improving the realism of the scavenging schemes (e.g., calculating separate liquid phase and mixed-phase precipitation production terms, tracking concentrations of gases dissolved in each hydrometeor type) and decreasing the horizontal grid spacing to improve the simulated amount of entrainment mixing.

5.2. CT With Liquid Water

We wish to evaluate the DC3 hypothesis that CTs vary among different storm types and affect the amount of scavenging and aqueous chemistry that occurs. Typical CTs with liquid water of an air parcel traveling through the convective cores were estimated for each storm using observational data and model output. CTs with liquid water derived from observations for above freezing and mixed-phase cloud regions were calculated as follows:

$$\mathrm{CT}_{\mathrm{obs}}(s) = \sum_{k=a}^{b} \frac{\Delta z_k}{w_k} \tag{4}$$

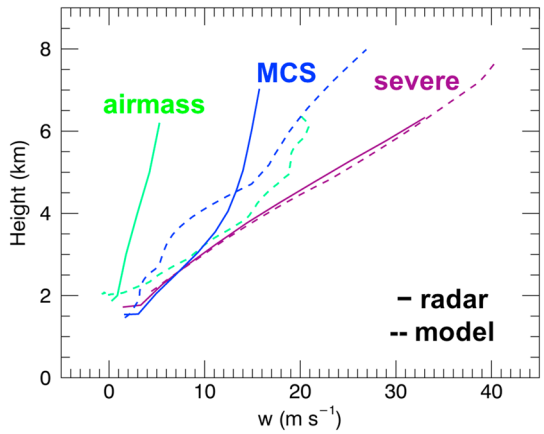

Figure 12. Vertical velocity profiles from the dual-polarimetric radar columns (solid lines) and WRF-Chem online trajectories (dashed lines) containing maximum updraft velocities at 23:00 UTC on 29 May 2012 for the severe (purple) and air mass (green) storms and the MCS (blue). WRF-Chem = Weather Research and Forecasting model with Chemistry; MCS = mesoscale convective system.

where a is the cloud base or 0°C level and b is the 0°C or −15°C level, respectively; Δz_k is the depth (m) of the radar grid cell at level k; and w_k is the vertical velocity (ms^{-1}) at level k. While supercooled water can be found at temperatures nearly as low as −40°C (Lawson et al., 2017; Rosenfeld & Woodley, 2000), we examine CTs to −15°C, the top of the scavenging region in WRF-Chem. Cloud base (lifting condensation level determined from skewT plot), 0°C, and −15°C heights were determined.

For each model trajectory that attained the minimum observed outflow altitude (severe storm: 10.34 km asl; air mass storm: 10.04 km asl; MCS: 11.85 km asl), the CTs with liquid water were determined as

$$\mathrm{CT}_{\mathrm{sim}}(s) = t_b - t_a \tag{5}$$

where t_b (s) is the time the trajectory is at the 0°C level or −15°C level and t_a (s) is the time the trajectory parcel is at cloud base or the 0°C level for above freezing and mixed-phase regions, respectively.

Both the observations and WRF-Chem simulations show CTs to be shortest for the severe storm (~6 min from cloud base to 0°C, 1.5 min from 0°C to −15 C, Figure 11). The CTs in the MCS are at least twice as long as in the severe storm, where WRF-Chem predicts 23 min from cloud base to 0°C and 4.5 min from 0°C to −15 °C and the TELEX observations give 16 min from cloud base to 0°C and 4.4 min from 0°C to −15°C. For the air mass storm, CTs from observations are longer (31 min from cloud base to 0°C and 14 min from 0°C to −15°C) than the WRF-Chem predictions (6.5 min from cloud base to 0°C and 2.7 min from 0°C to −15°C) and the estimates from observations and simulations for the other two storms. The shorter CTs predicted by WRF-Chem for the air mass storm are a result of higher simulated vertical velocities than observed (w_{max} between cloud base and −15°C of trajectory containing highest w_{max} = 20.9 ms^{-1}, Figure 12) compared with observations (w_{max} = 5.3 ms^{-1}). The overestimate in CT by WRF-Chem for the MCS may be due to lower simulated updraft velocities between cloud base and 0°C (Figure 12). The greatest uncertainty in the CT for the MCS is that the TELEX profile is for a different MCS and may not well represent the DC3 MCS. However, the higher-column-maximum reflectivities simulated by WRF-Chem relative to NEXRAD (Figure 1) suggest that WRF-Chem updraft velocities may indeed be higher than in the observed DC3 storm.

One of the hypotheses of DC3 was that storms with longer liquid water CTs (i.e., air mass versus severe storms) would have greater reductions in mixing ratios from cloud base to outflow due to more time available for microphysical scavenging and aqueous chemistry. However, we find that observed SEs are similar among storms for each species, despite liquid water CTs ranging from 7.5 to 45 min. The different liquid water CTs among the storms do not lead to significantly different scavenging sinks for the three species because (1) the shorter CTs in the severe storm than MCS than air mass storm are compensated by higher precipitation production rates and cloud water contents (Figure 8) in the severe versus air mass storm and MCS and (2) there are lower peroxide and CH_2O mixing ratios at cloud base for the air mass storm than the severe storm and MCS (Figure 3).

6. Conclusions

Aircraft measurements in inflow and outflow of deep convective storms over the central United States combined with high-resolution meteorology-chemistry simulations enable the quantification of storm processes affecting net convective transport of peroxides and CH_2O.

Our results complement the evidence in Bela et al. (2016) that CH_2O r_f values, determined by comparing the SEs calculated from WRF-Chem sensitivity simulations of the MCS with SEs obtained from aircraft observations, are <0.25. The simulated CH_3OOH SEs for the air mass storm and MCS were highly sensitive to the r_f value, indicating that ice retention is a significant component of CH_3OOH removal. On the other hand, for CH_2O and H_2O_2, r_f values greater than 0.5 and 0.25, respectively, result in simulated SEs greater than 90%, much higher than those calculated from observations.

However, the WRF-Chem simulations may overestimate rain and hail production, potentially affecting the confidence in the determined r_f values. For WRF-Chem simulations of all three storms, 35 dBZ volumes

Acknowledgments
We thank Paul O. Wennberg, John D. Crounse, Jason M. St. Clair, Alex P. Teng, Daniel O'Sullivan, L. Gregory Huey, Dexian Chen, Xiaoxi Liu, Donald Blake, Nicola Blake, Eric Apel, Rebecca S. Hornbrook, Frank Flocke, Teresa Campos, and Glenn Diskin for collecting the aircraft measurements used in this study. We also thank Dale Allen for feedback during the research process and Julie Lundquist for her helpful comments on the manuscript. We appreciate Marc Salzmann and an anonymous reviewer for their useful suggestions and comments, which improved the manuscript. M. M. Bela and O. B. Toon were supported by National Aeronautics and Space Administration (NASA) ACCDAMNNX14AR56G. M. M. Bela was also funded by a National Research Council Research Associateship Programs (NRC RAP) Postdoctoral Fellowship in the NOAA-ESRL Global Systems Division. The National Center for Atmospheric Research is sponsored by the National Science Foundation (NSF). A. Fried was supported by NSF and NASA under grants AGS-1261559 and NNX12AMO8G, respectively. C. Homeyer was funded by NSF grant AGS-1522910. The University of Maryland coauthors were supported under NSF grants 1063479 and 1522551. Q. Yang was supported by the Office of Science of the U.S. Department of Energy as part of the Atmospheric System Research Program (ASR). We acknowledge NCAR's Computational and Information Systems Laboratory (2016) for providing the Yellowstone supercomputer on which the simulations were conducted. We would like to thank Earth Networks for providing the ENTLN lightning data for research purposes. All the data used are listed in the references or archived at the following repositories: 1-s data merges from the NASA Langley DC3 Merged Aircraft Dataset Archive (http://www-air.larc.nasa.gov/cgi-bin/ArcView/dc3); NEXRAD data for individual radars from the National Climatic Data Center (NCDC; http://has.ncdc.noaa.gov/pls/plhas/has.dsselect); NSSL-MGAUS sounding data (http://data.eol.ucar.edu/codiac/dss/id=353.105); UAH Mobile Alabama sounding data (https://data.eol.ucar.edu/dataset/353.100); Jackson, MS sounding (http://weather.uwyo.edu/upperair/sounding.html); NCEP Stage IV precipitation analysis (https://data.eol.ucar.edu/cgi-bin/codiac/fgr_form/id=21.093); NAM-ANL (http://nomads.ncdc.noaa.gov/data/namanl/); GFS analyses and forecasts (https://www.ncdc.noaa.gov/data-access/model-data/model-datasets/global-forcast-system-gfs); MOZART chemical forecasts

(a proxy for graupel/hail volumes) of the main storm cores were much greater than those calculated from NEXRAD radar. For the air mass storm, simulated hail volumes were much greater than those from a dual-polarimetric radar analysis. Simulated maximum updraft velocities in the air mass storm were up to 4 times higher than from a dual-polarimetric radar analysis, further indicating the simulated storm was more severe than occurred. Mass concentrations of cloud water, rain, hail, and cloud ice simulated by WRF-Chem were generally higher than those calculated by a diabatic Lagrangian analysis model with input from time-dependent 3-D radar-analyzed wind and reflectivity fields. Since the amount of scavenging is determined by both the r_f value and the precipitation production rate, the true r_f values could be higher than determined from simulations (Bela et al., 2016 and this study) for CH_3OOH, which is affected by both liquid and mixed-phase scavenging, and CH_2O and H_2O_2, which are primarily scavenged by rain. We note that although the severe storm and MCS simulations use different microphysics schemes, the temperature ranges of peak precipitation production in the online WRF-Chem trajectories are similar among the three storm simulations. Therefore, we do not think the choice of microphysics schemes affects the relative contributions of above freezing and mixed-phase scavenging for these three storms.

We used output from WRF-Chem online trajectories to calculate the net effects of scavenging, entrainment, and aqueous chemistry on mixing ratios of CH_3OOH, CH_2O, and H_2O_2 at the $T = -15°C$ level, the lowest temperature at which mixed-phase scavenging is assumed to occur in the WRF-Chem scavenging scheme. This analysis was used to explain the results of Barth et al. (2016) and Bela et al. (2016) that CH_3OOH SEs were much higher than the expected values of <10% based on previous aircraft campaigns and the low solubility of CH_3OOH. In the severe storm and the MCS, more CH_3OOH is removed than expected, primarily due to depletion by entrainment. In the air mass storm, CH_3OOH and H_2O_2 SEs were lower than in the MCS, in part due to replenishment by entrainment of free tropospheric air. Measurements in other DC3 storms show that substantial mixing ratios of CH_3OOH are found in the midtroposphere (Barth et al., 2016). Although H_2O_2 has even higher midtropospheric mixing ratios, its much higher solubility than CH_3OOH means that entrainment of midtropospheric air has a smaller impact on outflow mixing ratios of H_2O_2 than CH_3OOH. Thus, although there is some variability in peroxide removal among storms with differing background profiles, in general, we expect CH_3OOH to be more affected than H_2O_2 by entrainment of background air. Above-freezing microphysical scavenging was the dominant process reducing CH_2O and H_2O_2 mixing ratios from cloud base to the top of the scavenging region in all three storms. Thus, liquid water CT does not affect SEs much because all three storms have sufficient CT to attain the potential amount of scavenging. Furthermore, aqueous chemistry sinks are so small that even a CT of 45 min in the air mass storm still does not result in significant reductions in peroxide mixing ratios.

The results of this study provide guidance for the development of model parameterizations of convective transport of gases affecting O_3 and aerosol distributions, and thus air quality and climate. Coordinated observations in inflow and outflow of different storms, including air mass storms in the Southeast United States, and in different regions of the world should be done to better quantify r_f. The WRF-Chem scavenging scheme is a simple approach that is computationally efficient yet allowed us to study removal processes inside deep convective clouds. In terms of model development, the WRF-Chem wet scavenging scheme could be improved by adding a parameterization for ice retention fraction, such as that proposed by Jost et al. (2017), in which r_f is a function of the effective Henry's law coefficient, accounting for chemical reactions such as the hydration of CH_2O whose rates are of similar time scales to mass transfer. Rather than use the total precipitation production rate to calculate wet removal, the individual production rates of rain, snow, and hail should be used so that different ice retention factors could be applied for dry growth riming (e.g.. $r_f = 0.59–0.97$ for H_2O_2 and CH_2O, Jost et al., 2017) and wet growth riming (e.g., $r_f < 0.2$ for H_2O_2 and CH_2O, Michael & Stuart, 2009).

References

Anbar, M., & Neta, P. (1967). A compilation of specific bimolecular rate constants for the reactions of hydrated electrons, hydrogen atoms and hydroxyl radicals with inorganic and organic compounds in aqueous solution. *The International Journal of Applied Radiation and Isotopes*, *18*(7), 493–523. https://doi.org/10.1016/0020-708X(67)90115-9

Barth, M. C., Bela, M. M., Fried, A., Wennberg, P. O., Crounse, J. D., St. Clair, J. M., et al. (2016). Convective transport and scavenging of peroxides by thunderstorms observed over the central U.S. during DC3. *Journal of Geophysical Research: Atmospheres*, *121*, 4272–4295. https://doi.org/10.1002/2015JD024570

Barth, M. C., Cantrell, C. A., Brune, W. H., Rutledge, S. A., Crawford, J. H., Huntrieser, H., et al. (2015). The Deep Convective Clouds and Chemistry (DC3) field campaign. *Bulletin of the American Meteorological Society*, *96*(8), 1281–1309. https://doi.org/10.1175/BAMS-D-13-00290.1

(https://www.acom.ucar.edu/WRF-Chem/mozart.shtml); NADP NTN (http://nadp.isws.illinois.edu/ntn/ntndata.aspx). The WRF-Chem code and land surface data are available for download from NCAR/MMM (http://www.mmm.ucar.edu/WRF/users/download/get_sources_wps_geog.html).

Barth, M. C., Kim, S.-W., Skamarock, W. C., Stuart, A. L., Pickering, K. E., & Ott, L. E. (2007). Simulations of the redistribution of formaldehyde, formic acid, and peroxides in the 10 July 1996 Stratospheric-Tropospheric Experiment: Radiation, Aerosols, and Ozone Deep Convection storm. *Journal of Geophysical Research*, *112*, D13310. https://doi.org/10.1029/2006JD008046

Barth, M. C., Sillman, S., Hudman, R., Jacobson, M. Z., Kim, C.-H., Monod, A., & Liang, J. (2003). Summary of the cloud chemistry modeling intercomparison: Photochemical box model simulation. *Journal of Geophysical Research*, *108*(D7), 4214. https://doi.org/10.1029/2002JD002673

Barth, M. C., Stuart, A. L., & Skamarock, W. C. (2001). Numerical simulations of the July 10, 1996, Stratospheric-Tropospheric Experiment: Radiation, Aerosols, and Ozone (STERAO)-Deep Convection experiment storm: Redistribution of soluble tracers. *Journal of Geophysical Research*, *106*(D12), 12,381–12,400. https://doi.org/10.1029/2001JD900139

Bela, M. M., Barth, M. C., Toon, O. B., Fried, A., Homeyer, C. R., Morrison, H., et al. (2016). Wet scavenging of soluble gases in DC3 deep convective storms using WRF-Chem simulations and aircraft observations. *Journal of Geophysical Research: Atmospheres*, *121*, 4233–4257. https://doi.org/10.1002/2015JD024623

Betts, A. K., Gatti, L. V., Cordova, A. M., Silva Dias, M. A. F., & Fuentes, J. D. (2002). Transport of ozone to the surface by convective downdrafts at night. *Journal of Geophysical Research*, *107*(D20), 8046. https://doi.org/10.1029/2000JD000158

Bielski, B. H. J. (1978). Reevaluation of the spectral and kinetic properties of HO_2 and O_2 free radicals. *Photochemistry and Photobiology*, *28*(45), 645–649. https://doi.org/10.1111/j.1751-1097.1978.tb06986.x

Biggerstaff, M. I., Wicker, L. J., Guynes, J., Ziegler, C., Straka, J. M., Rasmussen, E. N., et al. (2005). The Shared Mobile Atmospheric Research and Teaching Radar: A collaboration to enhance research and teaching. *Bulletin of the American Meteorological Society*, *86*(9), 1263–1274. https://doi.org/10.1175/BAMS-86-9-1263

Biggerstaff, M. I., Zounes, Z., Addison Alford, A., Carrie, G. D., Pilkey, J. T., Uman, M. A., & Jordan, D. M. (2017). Flash propagation and inferred charge structure relative to radar-observed ice alignment signatures in a small Florida mesoscale convective system. *Geophysical Research Letters*, *44*, 8027–8036. https://doi.org/10.1002/2017GL074610

Boccippio, D. J., Cummins, K. L., Christian, H. J., & Goodman, S. J. (2001). Combined satellite- and surface-based estimation of the intracloud–cloud-to-ground lightning ratio over the continental United States. *Monthly Weather Review*, *129*(1), 108–122. https://doi.org/10.1175/1520-0493(2001)129<0108:CSASBE>2.0.CO;2

Bothe, E., & Schulte-Frohlinde, D. (2014). Reaction of dihydroxymethyl radical with molecular oxygen in aqueous solution. *Zeitschrift für Naturforschung B*, *35*(8), 1035–1039.

Boyce, S. D., & Hoffmann, M. R. (1984). Kinetics and mechanism of the formation of hydroxymethanesulfonic acid at low pH. *The Journal of Physical Chemistry*, *88*(20), 4740–4746. https://doi.org/10.1021/j150664a059

Bryan, G. H., & Morrison, H. (2012). Sensitivity of a simulated squall line to horizontal resolution and parameterization of microphysics. *Monthly Weather Review*, *140*(1), 202–225. https://doi.org/10.1175/MWR-D-11-00046.1

Bryan, G. H., Wyngaard, J. C., & Fritsch, J. M. (2003). Resolution requirements for the simulation of deep moist convection. *Monthly Weather Review*, *131*(10), 2394–2416. https://doi.org/10.1175/1520-0493(2003)131<2394:RRFTSO>2.0.CO;2

Burkholder, J. B., Sander, S. P., Abbatt, J., Barker, J. R., Huie, R. E., Kolb, C. E., et al. (2015). Chemical kinetics and photochemical data for use in atmospheric studies, evaluation no. 18.

Chin, M., Ginoux, P., Kinne, S., Torres, O., Holben, B. N., Duncan, B. N., et al. (2002). Tropospheric aerosol optical thickness from the GOCART model and comparisons with satellite and sun photometer measurements. *Journal of the Atmospheric Sciences*, *59*(3), 461–483. https://doi.org/10.1175/1520-0469(2002)059<0461:TAOTFT>2.0.CO;2

Christensen, H., Sehested, K., & Corfitzen, H. (1982). Reactions of hydroxyl radicals with hydrogen peroxide at ambient and elevated temperatures. *The Journal of Physical Chemistry*, *86*(9), 1588–1590. https://doi.org/10.1021/j100206a023

Cohan, D. S., Schultz, M. G., Jacob, D. J., Heikes, B. G., & Blake, D. R. (1999). Convective injection and photochemical decay of peroxides in the tropical upper troposphere: Methyl iodide as a tracer of marine convection. *Journal of Geophysical Research*, *104*(D5), 5717–5724. https://doi.org/10.1029/98JD01963

Computational and Information Systems Laboratory (2016). Yellowstone: IBM iDataPlex System (NCAR Community Computing).

DeCaria, A. J., Pickering, K. E., Stenchikov, G. L., & Ott, L. E. (2005). Lightning-generated NO_x and its impact on tropospheric ozone production: A three-dimensional modeling study of a stratosphere-troposphere experiment: Radiation, aerosols and ozone (STERAO-A) thunderstorm. *Journal of Geophysical Research*, *110*, D14303. https://doi.org/10.1029/2004JD005556

DiGangi, E. A., MacGorman, D. R., Ziegler, C. L., Betten, D., Biggerstaff, M., Bowlan, M., & Potvin, C. K. (2016). An overview of the 29 May 2012 Kingfisher supercell during DC3. *Journal of Geophysical Research: Atmospheres*, *121*(24), 14,316–14,343. https://doi.org/10.1002/2016JD025690

Elliot, A. J. (1989). A pulse radiolysis study of the temperature dependence of reactions involving H, OH and e^-_{aq} in aqueous solutions. *Radiation Physics and Chemistry*, *34*, 753–758. https://doi.org/10.1016/1359-0197(89)90279-8

Emmons, L. K., Walters, S., Hess, P. G., Lamarque, J.-F., Pfister, G. G., Fillmore, D., et al. (2010). Description and evaluation of the Model for Ozone and Related chemical Tracers, version 4 (MOZART-4). *Geoscientific Model Development*, *3*(1), 43–67. https://doi.org/10.5194/gmd-3-43-2010

Fast, J. D., Gustafson, W. I., Easter, R. C., Zaveri, R. A., Barnard, J. C., Chapman, E. G., et al. (2006). Evolution of ozone, particulates, and aerosol direct radiative forcing in the vicinity of Houston using a fully coupled meteorology-chemistry-aerosol model. *Journal of Geophysical Research*, *111*, D21305. https://doi.org/10.1029/2005JD006721

Fried, A., Barth, M., Bela, M., Weibring, P., Richter, D., Walega, J., et al. (2016). Convective transport of formaldehyde to the upper troposphere and lower stratosphere and associated scavenging in thunderstorms over the central United States during the 2012 DC3 study. *Journal of Geophysical Research: Atmospheres*, *121*, 7430–7460. https://doi.org/10.1002/2015JD024477

Gerken, T., Wei, D., Chase, R. J., Fuentes, J. D., Schumacher, C., Machado, L. A., et al. (2016). Downward transport of ozone rich air and implications for atmospheric chemistry in the Amazon rainforest. *Atmospheric Environment*, *124*, 64–76. https://doi.org/10.1016/j.atmosenv.2015.11.014

Grell, G. A., Peckham, S. E., Schmitz, R., McKeen, S. A., Frost, G., Skamarock, W. C., & Eder, B. (2005). Fully coupled "online" chemistry within the WRF model. *Atmospheric Environment*, *39*(37), 6957–6975. https://doi.org/10.1016/j.atmosenv.2005.04.027

Guenther, A., Karl, T., Harley, P., Wiedinmyer, C., Palmer, P. I., & Geron, C. (2006). Estimates of global terrestrial isoprene emissions using MEGAN (Model of Emissions of Gases and Aerosols from Nature). *Atmospheric Chemistry and Physics*, *6*(11), 3181–3210. https://doi.org/10.5194/acp-6-3181-2006

Herrmann, H., Reese, A., Ervens, B., Wicktor, F., & Zellner, R. (1999). Laboratory and modelling studies of tropospheric multiphase conversions involving some C1 and C2 peroxyl radicals. *Physics and Chemistry of the Earth, Part B: Hydrology, Oceans and Atmosphere*, *24*(3), 287–290. https://doi.org/10.1016/S1464-1909(98)00052-5

Hong, S.-Y., & Lim, J.-O. J. (2006). The WRF Single-Moment 6-Class Microphysics Scheme (WSM6). *Journal of the Korean Meteorological Society*, *42*(2), 129–151.

Hong, S.-Y., Noh, Y., & Dudhia, J. (2006). A new vertical diffusion package with an explicit treatment of entrainment processes. *Monthly Weather Review*, *134*(9), 2318–2341. https://doi.org/10.1175/MWR3199.1

Huie, R. E., & Neta, P. (1987). Rate constants for some oxidations of S(IV) by radicals in aqueous solutions. *Atmospheric Environment*, *21*(8), 1743–1747. https://doi.org/10.1016/0004-6981(87)90113-2

Iacono, M. J., Delamere, J. S., Mlawer, E. J., Shephard, M. W., Clough, S. A., & Collins, W. D. (2008). Radiative forcing by long-lived greenhouse gases: Calculations with the AER radiative transfer models. *Journal of Geophysical Research*, *113*, D13103. https://doi.org/10.1029/2008JD009944

Iribarne, J., & Pyshnov, T. (1990). The effect of freezing on the composition of supercooled droplets—I. Retention of HCl, HNO_3, NH_3 and H_2O_2. *Atmospheric Environment. Part A. General Topics*, *24*(2), 383–387. https://doi.org/10.1016/0960-1686(90)90118-7

Jacob, D. J. (1986). Chemistry of OH in remote clouds and its role in the production of formic acid and peroxymonosulfate. *Journal of Geophysical Research*, *91*(D9), 9807–9826. https://doi.org/10.1029/JD091iD09p09807

Jost, A., Szakáll, M., Diehl, K., Mitra, S. K., & Borrmann, S. (2017). Chemistry of riming: The retention of organic and inorganic atmospheric trace constituents. *Atmospheric Chemistry and Physics*, *17*(16), 9717–9732. https://doi.org/10.5194/acp-17-9717-2017

Lawson, P., Gurganus, C., Woods, S., & Bruintjes, R. (2017). Aircraft observations of cumulus microphysics ranging from the tropics to midlatitudes: Implications for a "new" secondary ice process. *Journal of the Atmospheric Sciences*, *74*(9), 2899–2920. https://doi.org/10.1175/JAS-D-17-0033.1

Le Henaff, P. (1968). Methodes d'etude et proprietes des hydrates, hemiacetals et hemiacetals derives des aldehydes et des cetones. *Bulletin de la Société Chimique de France*, 4687–4700.

Lebo, Z. J., & Morrison, H. (2015). Effects of horizontal and vertical grid spacing on mixing in simulated squall lines and implications for convective strength and structure. *Monthly Weather Review*, *143*(11), 4355–4375. https://doi.org/10.1175/MWR-D-15-0154.1

Lelieveld, J., & Crutzen, P. J. (1991). The role of clouds in tropospheric photochemistry. *Journal of Atmospheric Chemistry*, *12*(3), 229–267. https://doi.org/10.1007/BF00048075

Leriche, M., Pinty, J.-P., Mari, C., & Gazen, D. (2013). A cloud chemistry module for the 3-D cloud-resolving mesoscale model Meso-NH with application to idealized cases. *Geoscientific Model Development*, *6*(4), 1275–1298. https://doi.org/10.5194/gmd-6-1275-2013

Li, Y., Pickering, K. E., Allen, D. J., Barth, M. C., Bela, M. M., Cummings, K. A., et al. (2017). Evaluation of deep convective transport in storms from different convective regimes during the DC3 field campaign using WRF-Chem with lightning data assimilation. *Journal of Geophysical Research: Atmospheres*, *122*, 7140–7163. https://doi.org/10.1002/2017JD026461

Lin, Y.-L., Farley, R. D., & Orville, H. D. (1983). Bulk parameterization of the snow field in a cloud model. *Journal of Climate and Applied Meteorology*, *22*(6), 1065–1092. https://doi.org/10.1175/1520-0450(1983)022<1065:BPOTSF>2.0.CO;2

Lind, J. A., Lazrus, A. L., & Kok, G. L. (1987). Aqueous phase oxidation of sulfur(IV) by hydrogen peroxide, methylhydroperoxide, and peroxyacetic acid. *Journal of Geophysical Research*, *92*(D4), 4171–4177. https://doi.org/10.1029/JD092iD04p04171

Lund, N. R., MacGorman, D. R., Schuur, T. J., Biggerstaff, M. I., & Rust, W. D. (2009). Relationships between lightning location and polarimetric radar signatures in a small mesoscale convective system. *Monthly Weather Review*, *137*(12), 4151–4170. https://doi.org/10.1175/2009MWR2860.1

MacGorman, D. R., Rust, W. D., Ziegler, C. L., Mansell, E. R., Schuur, T. J., Biggerstaff, M. I., et al. (2008). TELEX The Thunderstorm Electrification and Lightning Experiment. *Bulletin of the American Meteorological Society*, *89*(7), 997–1013. https://doi.org/10.1175/2007BAMS2352.1

Madronich, S. (1987). Photodissociation in the atmosphere: 1. Actinic flux and the effects of ground reflections and clouds. *Journal of Geophysical Research*, *92*(D8), 9740–9752. https://doi.org/10.1029/JD092iD08p09740

Mari, C., Jacob, D. J., & Bechtold, P. (2000). Transport and scavenging of soluble gases in a deep convective cloud. *Journal of Geophysical Research*, *105*(D17), 22,255–22,267. https://doi.org/10.1029/2000JD900211

Martini, M., Allen, D. J., Pickering, K. E., Stenchikov, G. L., Richter, A., Hyer, E. J., & Loughner, C. P. (2011). The impact of North American anthropogenic emissions and lightning on long-range transport of trace gases and their export from the continent during summers 2002 and 2004. *Journal of Geophysical Research*, *116*, D07305. https://doi.org/10.1029/2010JD014305

McArdle, J. V., & Hoffmann, M. R. (1983). Kinetics and mechanism of the oxidation of aquated sulfur dioxide by hydrogen peroxide at low pH. *The Journal of Physical Chemistry*, *87*(26), 5425–5429. https://doi.org/10.1021/j150644a024

Mecikalski, R. M., Bain, A. L., & Carey, L. D. (2015). Radar and lightning observations of deep moist convection across northern Alabama during DC3: 21 May 2012. *Monthly Weather Review*, *143*, 2774–2794. https://doi.org/10.1175/MWR-D-14-00250.1

Michael, R., & Stuart, A. L. (2009). The fate of volatile chemicals during wet growth of a hailstone. *Environmental Research Letters*, *4*(1).

Morrison, H., Curry, J. A., & Khvorostyanov, V. I. (2005). A new double-moment microphysics parameterization for application in cloud and climate models. Part i: Description. *Journal of the Atmospheric Sciences*, *62*(6), 1665–1677. https://doi.org/10.1175/JAS3446.1

Morrison, H., Thompson, G., & Tatarskii, V. (2009). Impact of cloud microphysics on the development of trailing stratiform precipitation in a simulated squall line: Comparison of one- and two-moment schemes. *Monthly Weather Review*, *137*(3), 991–1007. https://doi.org/10.1175/2008MWR2556.1

Neta, P., Huie, R. E., & Ross, A. B. (1988). Rate constants for reactions of inorganic radicals in aqueous solution. *Journal of Physical and Chemical Reference Data*, *17*(3), 1027–1284. https://doi.org/10.1063/1.555808

Neu, J. L., & Prather, M. J. (2012). Toward a more physical representation of precipitation scavenging in global chemistry models: Cloud overlap and ice physics and their impact on tropospheric ozone. *Atmospheric Chemistry and Physics*, *12*(7), 3289–3310. https://doi.org/10.5194/acp-12-3289-2012

Perrin, D. D. (2013). *Ionisation constants of inorganic acids and bases in aqueous solution* (2nd ed.). Burlington, MA: Elsevier Science.

Phoenix, D. B., Homeyer, C. R., & Barth, M. C. (2017). Sensitivity of simulated convection-driven stratosphere-troposphere exchange in WRF-Chem to the choice of physical and chemical parameterization. *Earth and Space Science*, *4*(8), 454–471. https://doi.org/10.1002/2017EA000287

Potvin, C. K., Wicker, L. J., & Shapiro, A. (2012). Assessing errors in variational dual-Doppler wind syntheses of supercell thunderstorms observed by storm-scale mobile radars. *Journal of Atmospheric and Oceanic Technology*, *29*(8), 1009–1025. https://doi.org/10.1175/JTECH-D-11-00177.1

Price, C., & Rind, D. (1992). A simple lightning parameterization for calculating global lightning distributions. *Journal of Geophysical Research*, *97*(D9), 9919–9933. https://doi.org/10.1029/92JD00719

Rosenfeld, D., & Woodley, W. L. (2000). Deep convective clouds with sustained supercooled liquid water down to −37.5°C. *Nature*, *405*(6785), 440–442.

Salzmann, M., Lawrence, M. G., Phillips, V. T. J., & Donner, L. J. (2007). Model sensitivity studies regarding the role of the retention coefficient for the scavenging and redistribution of highly soluble trace gases by deep convective cloud systems. *Atmospheric Chemistry and Physics*, *7*(8), 2027–2045. https://doi.org/10.5194/acp-7-2027-2007

Seinfeld, J. H., & Pandis, S. N. (2006). *Atmospheric Chemistry and Physics: From Air Pollution to Climate Change (2nd ed.)*. New York: John Wiley & Sons.

Skamarock, W. C. (2004). Evaluating mesoscale NWP models using kinetic energy spectra. *Monthly Weather Review*, *132*(12), 3019–3032. https://doi.org/10.1175/MWR2830.1

Smith, R. M., & Martell, A. E. (1974). *Critical stability constants*. London, New York: Plenum Press.

Snider, J. R., & Huang, J. (1998). Factors influencing the retention of hydrogen peroxide and molecular oxygen in rime ice. *Journal of Geophysical Research*, *103*(D1), 1405–1415. https://doi.org/10.1029/97JD02847

Snider, J. R., Montague, D. C., & Vali, G. (1992). Hydrogen peroxide retention in rime ice. *Journal of Geophysical Research*, *97*(D7), 7569–7578. https://doi.org/10.1029/92JD00237

Snow, J. A., Heikes, B. G., Shen, H., O'Sullivan, D. W., Fried, A., & Walega, J. (2007). Hydrogen peroxide, methyl hydroperoxide, and formaldehyde over North America and the North Atlantic. *Journal of Geophysical Research*, *112*, D12S07. https://doi.org/10.1029/2006JD007746

Staehelin, J., & Hoigne, J. (1982). Decomposition of ozone in water: rate of initiation by hydroxide ions and hydrogen peroxide. *Environmental Science & Technology*, *16*(10), 676–681. https://doi.org/10.1021/es00104a009

Sukoriansky, S., Galperin, B., & Perov, V. (2005). Application of a new spectral theory of stably stratified turbulence to the atmospheric boundary layer over sea ice. *Boundary-Layer Meteorology*, *117*(2), 231–257. https://doi.org/10.1007/s10546-004-6848-4

Taylor, J. R. (1982). *An introduction to error analysis: The study of uncertainties in physical measurements*. Mill Valley, CA: University Science Books.

Tie, X., Madronich, S., Walters, S., Zhang, R., Rasch, P., & Collins, W. (2003). Effect of clouds on photolysis and oxidants in the troposphere. *Journal of Geophysical Research*, *108*(D20), 4642. https://doi.org/10.1029/2003JD003659

Voisin, D., Legrand, M., & Chaumerliac, N. (2000). Scavenging of acidic gases (HCOOH, CH_3COOH, HNO_3, HCl, and SO_2) and ammonia in mixed liquid-solid water clouds at the Puy de Dôme mountain (France). *Journal of Geophysical Research*, *105*(D5), 6817–6835. https://doi.org/10.1029/1999JD900983

von Blohn, N., Diehl, K., Mitra, S. K., & Borrmann, S. (2011). Wind tunnel experiments on the retention of trace gases during riming: Nitric acid, hydrochloric acid, and hydrogen peroxide. *Atmospheric Chemistry and Physics*, *11*(22), 11,569–11,579. https://doi.org/10.5194/acp-11-11569-2011

von Blohn, N., Diehl, K., Nölscher, A., Jost, A., Mitra, S. K., & Borrmann, S. (2013). The retention of ammonia and sulfur dioxide during riming of ice particles and dendritic snow flakes: Laboratory experiments in the Mainz vertical wind tunnel. *Journal of Atmospheric Chemistry*, *70*(2), 131–150. https://doi.org/10.1007/s10874-013-9261-x

Wiedinmyer, C., Akagi, S. K., Yokelson, R. J., Emmons, L. K., Al-Saadi, J. A., Orlando, J. J., & Soja, A. J. (2011). The Fire IN ventory from NCAR (FINN): A high resolution global model to estimate the emissions from open burning. *Geoscientific Model Development*, *4*(3), 625–641. https://doi.org/10.5194/gmd-4-625-2011

Wine, P. H., Tang, Y., Thorn, R. P., Wells, J. R., & Davis, D. D. (1989). Kinetics of aqueous phase reactions of the SO_4 radical with potential importance in cloud chemistry. *Journal of Geophysical Research*, *94*(D1), 1085–1094. https://doi.org/10.1029/JD094iD01p01085

Yang, Q., Easter, R. C., Campuzano-Jost, P., Jimenez, J. L., Fast, J. D., Ghan, S. J., et al. (2015). Aerosol transport and wet scavenging in deep convective clouds: A case study and model evaluation using a multiple passive tracer analysis approach. *Journal of Geophysical Research: Atmospheres*, *120*, 8448–8468. https://doi.org/10.1002/2015JD023647

Ziegler, C. L. (2013a). A diabatic Lagrangian technique for the analysis of convective storms. Part I: Description and validation via an observing system simulation experiment. *Journal of Atmospheric and Oceanic Technology*, *30*(10), 2248–2265. https://doi.org/10.1175/JTECH-D-12-00194.1

Ziegler, C. L. (2013b). A diabatic Lagrangian technique for the analysis of convective storms. Part II: Application to a Radar-observed storm. *Journal of Atmospheric and Oceanic Technology*, *30*(10), 2266–2280. https://doi.org/10.1175/JTECH-D-13-00036.1

Ziegler, C. L. (2013c). NSSL MGAUS Oklahoma-Texas Sounding data, version 1.0, UCAR/NCAR - Earth Ob. Lab. Retrieved from http://data.eol.ucar.edu/dataset/353.105, Accessed 06 Jun. 2014.